Universiteit Antwerpen

This item is the archived peer-reviewed author-version of:

Incommensurate modulations and perovskite growth in $La_xSr_{2-x}MnO_{4-\delta}$ affecting solid oxide fuel cell conductivity

Reference:
Vandemeulebroucke Daphne, Batuk Maria, Hajizadeh Amirhossein, Wastiaux Myriam, Roussel Pascal, Hadermann Joke.- Incommensurate modulations and perovskite growth in $La_xSr_{2-x}MnO_{4-\delta}$ affecting solid oxide fuel cell conductivity
Chemistry of materials / American Chemical Society - ISSN 1520-5002 - 36:5(2024), p. 2441-2449
Full text (Publisher's DOI): https://doi.org/10.1021/ACS.CHEMMATER.3C03199
To cite this reference: https://hdl.handle.net/10067/2043540151162165141

uantwerpen.be
Institutional repository IRUA

Incommensurate Modulations and Perovskite Growth in $La_xSr_{2-x}MnO_{4-\delta}$ Affecting Solid Oxide Fuel Cell Conductivity

Daphne Vandemeulebroucke,*,† Maria Batuk,† Amirhossein Hajizadeh,† Myriam Wastiaux,‡ Pascal Roussel,‡ and Joke Hadermann†

† *EMAT, University of Antwerp, Groenenborgerlaan 171, 2020 Antwerpen, Belgium*

‡*UCCS, University of Lille, CNRS UMR8181, Avenue Mendeleiev, 59655 Villeneuve d'Ascq Cedex, France*

E-mail: daphne.vandemeulebroucke@uantwerpen.be

Abstract

Ruddlesden-Popper $La_xSr_{2-x}MnO_{4-\delta}$ materials are interesting symmetric solid oxide fuel cell electrodes due to their good redox stability, mixed ionic and electronic conducting behavior and thermal expansion that matches well with common electrolytes. In reducing environments - as at a solid oxide fuel cell anode - the x = 0.5 member, i.e. $La_{0.5}Sr_{1.5}MnO_{4-\delta}$, has a much higher total conductivity than compounds with a different La/Sr ratio, although all those compositions have the same K_2NiF_4-type I4/mmm structure. The origin for this conductivity difference is not yet known in literature. Now, a combination of in-situ and ex-situ 3D electron diffraction, high-resolution imaging, energy-dispersive X-ray analysis and electron energy-loss spectroscopy uncovered clear differences between x=0.25 and x=0.5 in the pristine structure, as well as in the transformations upon high-temperature reduction. In $La_{0.5}Sr_{1.5}MnO_{4-\delta}$, Ruddlesden-Popper n=2 layer defects and an amorphous surface layer are present, but not in

$La_{0.25}Sr_{1.75}MnO_{4-\delta}$. After annealing at 700°C in 5% H_2/Ar, $La_{0.25}Sr_{1.75}MnO_{4-\delta}$ transforms to a tetragonal 2D incommensurately modulated structure with modulation vectors $\vec{q}_1 = 0.2848(1) \cdot (\vec{a}^* + \vec{b}^*)$ and $\vec{q}_2 = 0.2848(1) \cdot (\vec{a}^* - \vec{b}^*)$, whereas $La_{0.5}Sr_{1.5}MnO_{4-\delta}$ only partially transforms to an orthorhombic 1D incommensurately modulated structure, with $\vec{q} = 0.318(2) \cdot \vec{c}^*$. Perovskite domains grow at the crystal edge at 700°C in 5% H_2 or vacuum, due to the higher La concentration on the surface compared to the bulk, which leads to a different thermodynamic equilibrium. Since it is known that a lower degree of oxygen vacancy ordering and a higher amount of perovskite blocks enhance oxygen mobility, those differences in defect structure and structural transformation upon reduction, might all contribute to the higher conductivity of $La_{0.5}Sr_{1.5}MnO_{4-\delta}$ in solid oxide fuel cell anode conditions compared to other La/Sr ratios.

Introduction

In solid oxide fuel cells (SOFC), electricity is generated by means of redox reactions, requiring oxygen at the cathode and a fuel - e.g. methane or hydrogen gas - at the anode. Their electrolytes are solid ceramics with ionic conductivities that increase with temperature. Therefore, the first SOFCs could only operate at very high temperatures: from 750°C to 1000°C. Since then, many efforts have been made to reduce the performance temperature, and intermediate-temperature SOFCs have been created, working between 500°C and 750°C.[1] One way to optimize the performance, is the use of Mixed Ionic and Electronic Conductors (MIEC) as electrode materials, since they exhibit both electron and oxide ion mobility.[2] A particular group of MIECs for symmetric SOFCs - where the cathode and the anode consist of the same material - are the Ruddlesden-Popper (RP) manganites $La_xSr_{2-x}MnO_{4-\delta}$. This series structurally belongs to the layered K_2NiF_4 -type RP materials, which can be derived from a perovskite oxide with general formula ABO_3 (Figure 1a). RP oxides consist of an alternation between one rock salt layer AO and n perovskite layers ABO_3, leading to the general formula $A_{n+1}B_nO_{3n+1}$ or $(AO)(ABO_3)_n$ with n = 1, 2, 3, ... (Figure 1). For the

particular composition $La_xSr_{2-x}MnO_4$ with $0 \leq x \leq 1$ and space group I4/mmm, only one perovskite layer is situated in between the rock salt layers ($n = 1$), as illustrated in Figure 1b.

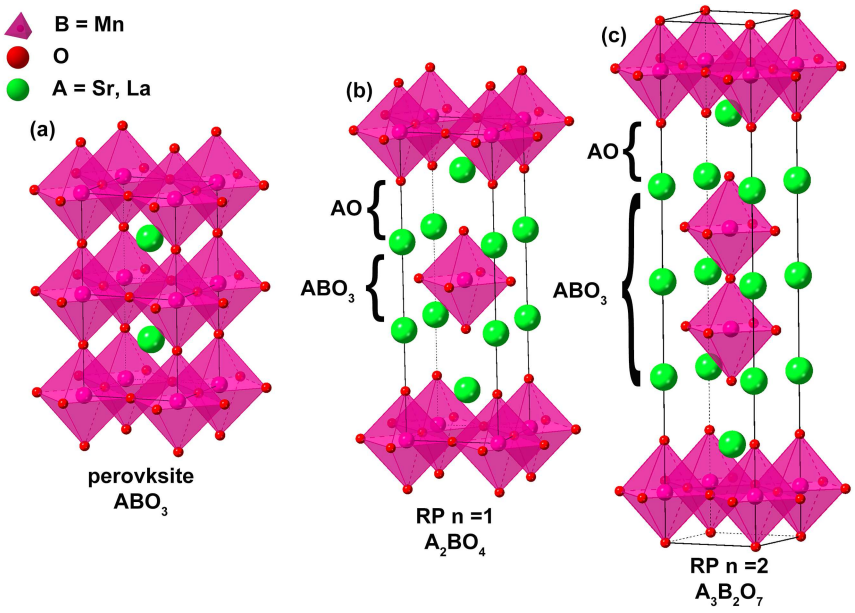

Figure 1: Schematic representation of a single perovskite with chemical formula $AMnO_3$ (a) and Ruddlesden-Popper structures A_2MnO_4 with $n = 1$ (b) and $A_3Mn_2O_7$ with $n = 2$ (c). Here, A is Sr or La, and B is Mn.

It was reported that the $La_xSr_{2-x}MnO_{4-\delta}$ compositions with $0 \leq x \leq 1.4$ have comparable thermal expansion properties to most common electrolytes, and possess a good stability up to 800°C in air, which is crucial for their performance as a SOFC cathode.[3] Moreover, symmetric SOFCs also require stability in reducing conditions. In-situ powder X-ray diffraction (XRD) and neutron diffraction (ND) showed that $La_xSr_{2-x}MnO_{4-\delta}$ with $0.25 \leq x \leq 0.6$ remains stable under flowing hydrogen gas, as in the operational environment at the anode. From this series, $La_{0.5}Sr_{1.5}MnO_{4-\delta}$ possesses the best combination of conductivities in oxidizing and reducing conditions at 800°C, i.e. 35.6 S cm $^{-1}$ (air) and 1.9 S cm $^{-1}$ (3% H_2/Ar). With these values, it breaks the decreasing (in air) and increasing (in hydrogen gas) conductivity trends of the other compositions with increasing La content. For x= 0.25, 0.4 and 0.6, these are 38.6 S cm^{-1}, 33.6 S cm^{-1} and 28.8 S cm^{-1} in air, and 0.4 S cm^{-1}, 0.5 S

cm^{-1} and 0.8 S cm^{-1} in 3% H_2/Ar, all at 800°C.[4] The reasons for this were not yet uncovered.

On top of that, despite the reported space group stability for $0.25 \leq x \leq 0.6$, the in-situ powder XRD and ND experiments by Sandoval et al.[4] displayed complex cell parameter changes upon heating and cooling in reducing atmosphere, that could not be explained by thermal expansion only. During reduction by heating in diluted H_2, non-linear steep changes happen for cell parameters a and c between 500°C and 600°C, which are reversed between 250°C and 350°C upon reoxidizing in air. Further, the anisotropic atomic displacement parameters (ADP) gave anomalous values after heating in H_2: one component of the ellipsoid was significantly larger than expected for thermal expansions, which indicates a structural transformation that could not be further quantified by in-situ powder XRD or ND experiments.

Therefore, we investigated these compounds using single-crystal 3D electron diffraction (3DED). For 3DED, crystals of a few tens of nanometers - sizes from which X-rays and neutrons can only produce powder patterns - already suffice to obtain single-crystal diffraction data. We already showed[5] that in-situ electron diffraction can pick up oxygen vacancy ordering that was overlooked in in-situ XRD or ND experiments. But ordering of oxygen vacancies has a significant effect on ionic transport properties. For instance, for $SrCo_{0.8}B'_{0.2}O_{3-\delta}$ (with B'= Cr, Fe, Co, Cu) and for $La_{0.6}Sr_{0.4}CoO_{3-\delta}$, the transition from a low-temperature vacancy-ordered state to a high-temperature disordered perovskite leads to an increase in oxygen permeability with 5 to 6 orders of magnitude (up to $3\cdot 10^{-7}$ mol cm^{-2} s^{-1}).[6]

With this research, we investigated whether differences in structural order might explain the differences in SOFC electrode performance for $La_xSr_{2-x}MnO_{4-\delta}$ with different La content. In addition to 3DED, we also performed high-resolution high-angle annular dark field scanning

transmission electron microscopy (HAADF-STEM), energy-dispersive X-ray spectroscopy (EDX) and electron energy-loss spectroscopy (EELS) on pristine and high-temperature reduced $La_xSr_{2-x}MnO_{4-\delta}$ with x = 0, 0.25 and 0.5, both in-situ and ex-situ.

Results

To study potential ordering phenomena upon reduction, $La_xSr_{2-x}MnO_{4-\delta}$ with x = 0, 0.25 and 0.5 were annealed in diluted hydrogen atmosphere and examined with 3D electron diffraction (3DED), of which the results are shown in Figure 2. $La_{0.25}Sr_{1.75}MnO_{4-\delta}$ (I4/mmm, a = 3.8324(3) Å, c = 12.422(1) Å) was first annealed in N_2 at 550°C for 1h and then in 5% H_2/Ar at 700°C for 1h. The prior nitrogen heating cycle was performed to remove any potentially adsorbed water and other molecules from the surface, and did not lead to any structural changes from the pristine state - as checked by 3DED and powder X-ray diffraction (XRD). After the hydrogen treatment at 700°C, precession 3DED revealed the transformation to an incommensurate 2D modulated structure with cell parameters a = 3.8324(7) Å and c = 12.6725(5) Å, and superspace group I4/mmm($\alpha\alpha$0)0000(α-α0)0000 where α = 0.2848(1). Figure 2b, 2e and 2h, show the reconstructed hk0 and h0l sections from 3DED and the modulation vectors $\vec{q}_1$ and $\vec{q}_2$. A very similar (3+2)D structure was already found for oxygen deficient $LaSrCuO_{3.5}$ with in-zone electron diffraction by Hadermann et al.,[7] with a somewhat different modulation wavelength ($\alpha \approx 0.22$) where the modulation was driven by oxygen vacancy order. Starting from a similar model and using precession 3DED, we could dynamically refine the atomic positions, positional and occupancy modulation parameters and atomic displacement parameters for modulated $La_{0.25}Sr_{1.75}MnO_{4-\delta}$ to the values listed in the supplementary information. Precessing the electron beam and the method of dynamical refinement are crucial to deal with the effects of multiple scattering in electron diffraction. It must be noted that from the reflection conditions only, also I4mm, I422 or I4 would be possible space groups of the average structure. However, in a recent paper from Klar et al.,[8]

it was shown that dynamical refinement from 3DED data can derive an inversion center and determine the absolute configuration, based on a significant decrease in the R-value. For 2D modulated $La_{0.25}Sr_{1.75}MnO_{4-\delta}$, we compared the refinements of the average structure with I4/mmm, I4mm, I422 and I4, of which I4/mmm gave the lowest R-value (as listed in the supplementary information). In Figure 3, the Mn-O plane is shown for the $t = 0$, $u = 0$ section through five-dimensional space. Vacancy ordering occurs for the equatorial oxygen positions, and gives rise to an alternation between manganese octahedra and square pyramids. A graphical representation of the occupancy modulation function of the equatorial oxygen atoms has been included in the supplementary information. For $La_{0.5}Sr_{1.5}MnO_{4-\delta}$ (I4/mmm, $a = 3.86007(7)$ Å, $c = 12.4135(5)$ Å), the identical heat treatment leads to a 1D incommensurate modulation, with a slightly longer modulation wave vector $\vec{q} = \alpha\ \vec{c}^*$ with $\alpha = 0.318(2)$, an orthorhombic superspace group Fmmm(0,0,α)000 and cell parameters $a = 5.4537(6)$ Å, $b = 12.711(2)$ Å and c =5.4403(5) Å (rotated 45° along the c axis with respect to the I4/mmm parent cell). Again, based on the reflection conditions, also Fmm2, Fm2m, F2mm and F222 could be possible. Since the data quality did not allow dynamical refinement here, we opted for the highest symmetry as the most likely case, as common in X-ray crystallography. For the x = 0.5 composition, the satellites are much weaker than for the x = 0.25 composition (and even weaker after hydrogen treatment without the N_2 cycle), as can be seen in Figure 2c, 2f and 2i. For this particular crystal, some weak reflections also appear along the $\vec{a}^*$ direction in the h0l section, but they stem from twinning and this composition is not two-dimensionally modulated. First, such reflections are not systematically present in all crystals. Moreover, no satellites are observed that arise from the combination of two different q vectors as e.g. in the h0l section of 2D modulated $La_{0.25}Sr_{1.75}MnO_{4-\delta}$ (Figure 2h). As a reference sample, also Sr_2MnO_4 (I4/mmm, $a = 3.78839(6)$ Å and $c = 12.4955(3)$ Å) was annealed in 5% H_2/Ar at 550°C for 1h, with prior N_2 heating cycle as described above. This caused a conversion to the known $P2_1/c$ superstructure of $Sr_2MnO_{3.5}$ as expected from literature[9,10] with $a = 6.82(1)$ Å, $b = 10.89(1)$ Å, $c = 10.95(2)$ Å and β

= 113.5(2)°, as in Figure 2a, 2d and 2g (main reflections in I4/mmm in white, two twins of $P2_1/c$ in yellow and green). The cell declared in the original paper is $a = \frac{1}{2}(-a_t - b_t + c_t)$, $b = 2(-a_t + b_t)$, $c = 2(a_t + b_t)$ (with the index t referring to the tetragonal subcell). The latter two equations correspond to a two-dimensional commensurate modulation with vectors $q_1 = \alpha\ (-\vec{a_t}^* + \vec{b_t}^*)$ and $q_2 = \alpha\ (\vec{a_t}^* + \vec{b_t}^*)$ where $\alpha = 0.25$, similar to the one we observe for $La_{0.25}Sr_{1.75}MnO_{4-\delta}$, but commensurate instead of incommensurate. Therefore, that cell could be described by a supercell in the original paper. The first equation implies an additional shift of the whole vacancy ordered layer over $\frac{1}{2}(-a_t - b_t + c_t)$. Due to the glide plane perpendicular to c_t with a translation along $a_t + b_t$, satellites in the $\vec{a}_t^* + \vec{b}_t^*$ direction are extinct (Figure 2d). Additionally, two more compositions with higher lanthanum content x = 0.75 and x = 1, i.e. $La_{0.75}Sr_{1.25}MnO_{4-\delta}$ (I4/mmm, a =3.81784(4) Å and c = 12.9040(3) Å) and $LaSrMnO_{4-\delta}$ (I4/mmm, a = 3.81624(2) Å and c = 13.1324(2) Å) were heated to 700°C in 5% H_2/Ar after a prior nitrogen cycle at 550°C. This gave the cell parameters a =3.8224(2) Å and c = 12.84(1) Å for $La_{0.75}Sr_{1.25}MnO_{4-\delta}$, and a =3.80592(7) Å and c = 13.1152(4) Å for $LaSrMnO_{4-\delta}$, but did not lead to any structural change to the space group observable by 3DED.

In pristine $La_{0.5}Sr_{1.5}MnO_{4-\delta}$, high-resolution high-angle annular dark field scanning transmission electron microscopy (HAADF-STEM) detects the systematic presence of an amorphous surface layer of 2-3 nm (Figure 4a, red arrow). Energy-dispersive X-ray spectroscopy (EDX) confirms the amorphous layer is indeed a lanthanum strontium manganite, but the relative lanthanum concentration of this layer is $\langle La/Sr \rangle$ = 1.0 (σ = 0.1), which is more than twice as large as in the bulk RP n = 1 structure: $\langle La/Sr \rangle$ = 0.36 (σ = 0.03) (Figure 4b). Note that for the quantification of the composition of the bulk RP n=1 structure, only non-oriented low magnification maps where taken into account. This is because quantification of EDX (as for EELS) of in-zone-oriented crystals is unreliable due to the excitation of guided light modes and relativistic losses.[11] Additionally, many higher order RP n = 2 layer

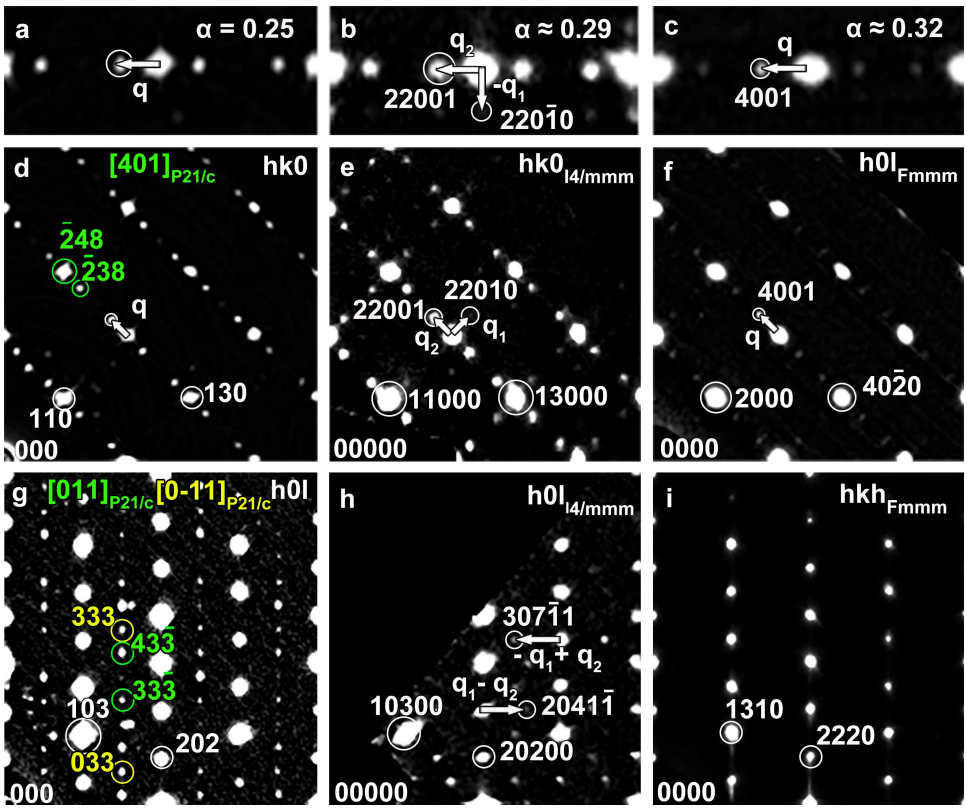

Figure 2: Reconstructed hk0, h0l and hkh sections from 3DED for annealed $La_xSr_{2-x}MnO_{4-\delta}$ at 700°C in 5% H_2/Ar with x = 0 (d, g), 0.25 (e, h) and 0.5 (f, i). The q vectors are indicated by arrows. Two twins of $P2_1/c$ are indexed in green and yellow. In a-c, details from the hk0 or h0l sections in d-f are given to illustrate the trend in the modulation wavelength. α is 0.25, 0.29 and 0.32 for x = 0, 0.25 and 0.5 respectively.

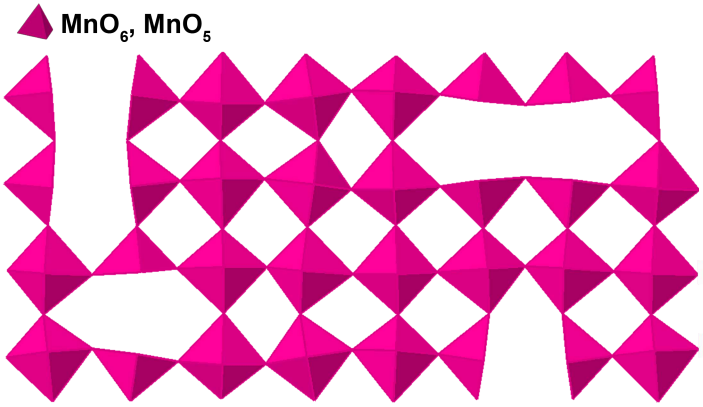

Figure 3: Schematic representation of the manganese coordination for the $t = 0$, $u = 0$ section through five-dimensional space of reduced $La_{0.25}Sr_{1.75}MnO_{4-\delta}$, seen along c. A threshold of 56% is applied to plot the oxygen position as filled. The vacancy ordering causes a pattern of octahedra and square pyramids.

defects were observed in the pristine material - at the surface and in the bulk area - that also contain relatively more lanthanum than the $n = 1$ structure. This can e.g. be seen by the brighter Z-contrast of the A cation layer in between the two perovskite layers in Figure 4c, and in the EDX map in Figure 4d. In some pristine $La_{0.5}Sr_{1.5}MnO_{4-\delta}$ crystals, perovskite blocks (La,Sr)MnO_3 are present that epitaxially grew during synthesis on the {001} face of the RP n =1 phase (Figure 4c) and also have a higher lanthanum content than the n=1 RP bulk (Figure 4d).

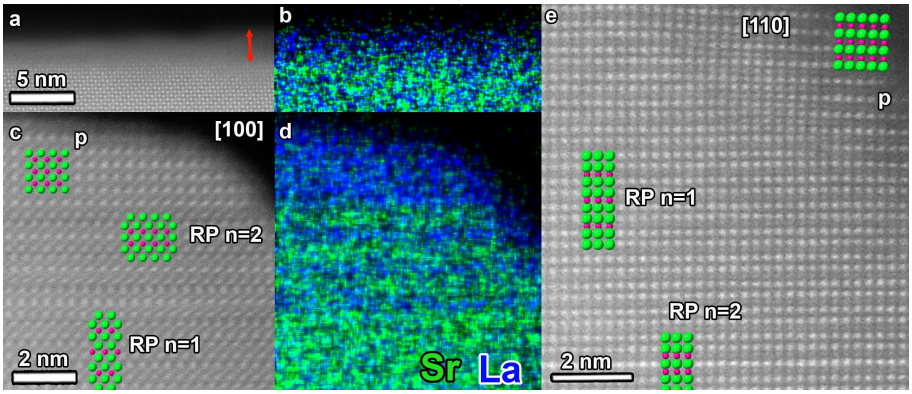

Figure 4: a-d: HAADF-STEM images and EDX maps (in counts) of pristine $La_{0.5}Sr_{1.5}MnO_{4-\delta}$. In the EDX maps, lanthanum is represented as blue, strontium as green. In the models on top of the high-resolution images, La/Sr atoms are shown in green, Mn atoms in pink. (a,b) An amorphous layer is visible at the surface (red arrow) with a higher La content than the bulk structure, while (c,d) some crystals show perovskite on the edge, and many show Ruddlesden-Popper (RP) $n = 2$ layer defects, both in the bulk as at the surface. All areas deviating from RP $n = 1$ are La-rich. e: HAADF-STEM image of the [110] section of $La_{0.5}Sr_{1.5}MnO_{4-\delta}$, first annealed at 550°C in N_2 and then at 700°C in 5% H_2/Ar. Perovskite domains are observed here as well, but instead of sharp domain boundaries, a distorted transition region of up to 2 nm is present.

After annealing $La_{0.5}Sr_{1.5}MnO_{4-\delta}$ in N_2 and in 5% H_2/Ar as described above, high-resolution HAADF-STEM also revealed many perovskite (La,Sr)MnO_3 domains on the surface of the crystals, as illustrated in Figure 4e. However, those domains are not as sharply demarcated as the perovskite regions in the pristine sample: instead of sharp domain boundaries, distorted "transition regions" are present, up to 2 nm in width. To determine the relation between the features in the pristine crystals and those after reduction, we used in-situ transmission

electron microscopy (TEM), which allows to follow single crystals throughout the reduction reaction.

Using a closed cell, $La_{0.5}Sr_{1.5}MnO_{4-\delta}$, $La_{0.25}Sr_{1.75}MnO_{4-\delta}$ and $Sr_2MnO_{4-\delta}$ were studied with in-situ 3DED using the same reduction treatment in diluted hydrogen gas as above, both with and without prior nitrogen cycle. However, none of the crystals exhibited the satellites observed after the ex-situ reduction. The reason for this is the formation of an unexpected silica shell around the crystals during the in-situ reaction, as revealed by EDX and electron energy-loss spectroscopy (EELS) (see e.g. Figure 5). This shell originates from Si migration to the crystals from the electron transparent silicon nitride window of the in-situ heating chips, hindering the reduction of the sample and the formation of a modulated structure. Most likely, the oxygen in SiO_2 stems from the sample, out of which it diffuses during heating. Nevertheless, the formation of a perovskite phase takes place here for both the x = 0.25 and the x = 0.5 compounds. This is evidenced by reflections in the 3DED patterns in agreement with a (La,Sr)MnO_3 perovskite structure with a $\approx$ 3.9 Å. Figure 6 shows the hk0 and 0kl reconstructed sections from the same $La_{0.5}Sr_{1.5}MnO_{4-\delta}$ crystal (Figure 6a, b, d, e) and $La_{0.25}Sr_{1.75}MnO_{4-\delta}$ crystal (Figure 6g, h) at room temperature before heating and at 700°C in 5% H_2/Ar (after the heating cycle in nitrogen). Reoxidation by another heating cycle in 20% O_2 or cooling in 20% O_2 to room temperature did not recover the original RP n = 1 structure, so - at least in the presence of the silica shell - the perovskite formation is not reversible. However, the undoped x = 0 composition did not show any perovskite reflections upon in-situ reduction.

Due to the extra reaction with the silicon nitride window, these in-situ results cannot be used to represent the actual circumstances as found in the applications. Several attempts were made to prevent the formation of the silica shell and to obtain an effective reduction in-situ in the closed cell, unfortunately without success. Details of these attempts can be

found in the Supporting Information.

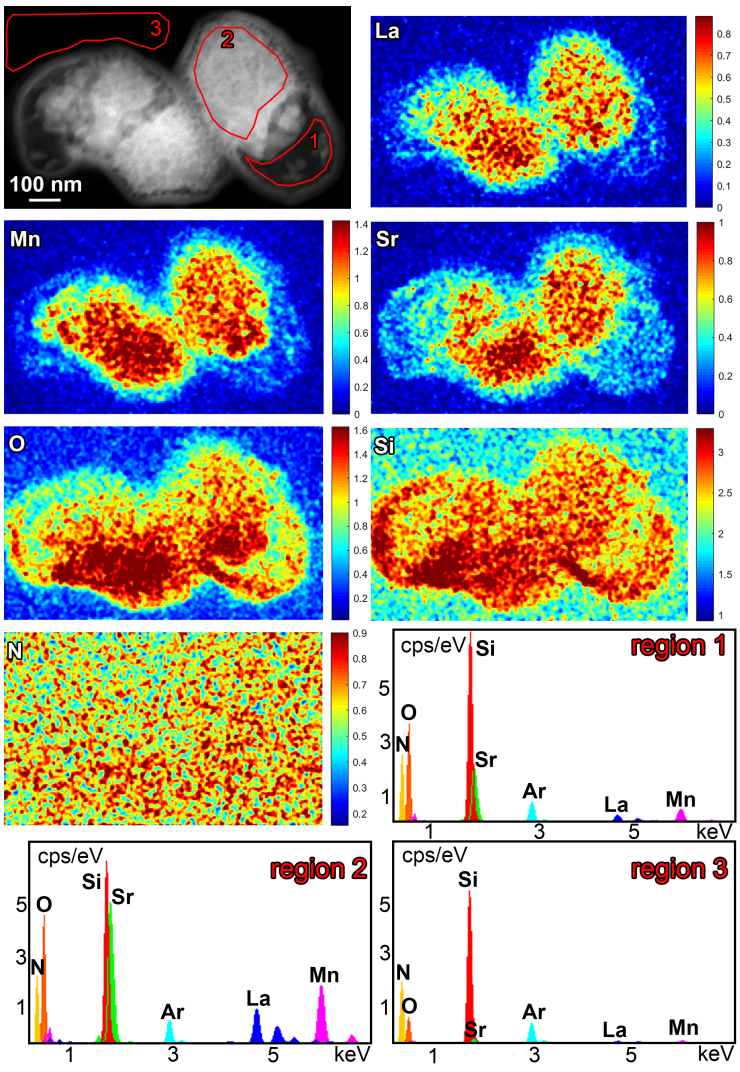

Figure 5: HAADF-STEM image and elemental EDX maps of two $La_{0.5}Sr_{1.5}MnO_{4-\delta}$ crystals after in-situ heating to 700°C in 5%H_2/Ar. All maps are given in counts. On the bottom, the deconvoluted EDX spectra are shown for three regions indicated in red on the HAADF-STEM image. The Ar peak is from the gas environment, N and a part of the Si stem from the support window. A silica shell is formed around the crystals.

To circumvent this shell formation, and still be able to follow the transformation, we turned to in-situ heating in vacuum, which is well-known to be a reducing atmosphere as well. As a test, the reference sample Sr_2MnO_4 was successfully reduced to $Sr_2MnO_{3.5}$ at 550°C in vacuum, as its $P2_1/c$ superstructure could be observed by in-situ 3DED. Next, $La_{0.5}Sr_{1.5}MnO_{4-\delta}$

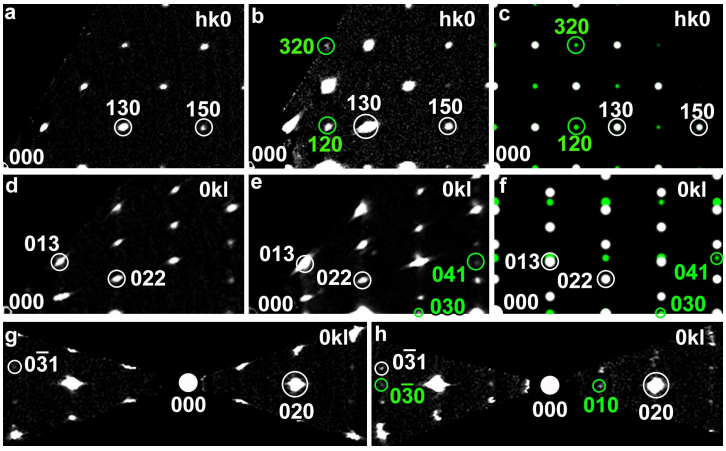

Figure 6: Experimental reconstructed hk0 and 0kl sections from 3DED and simulations. $La_{0.5}Sr_{1.5}MnO_{4-\delta}$ at room temperature in the pristine state in air (a, d) and at 700°C in 5% H_2/Ar (b, e). $La_{0.25}Sr_{1.75}MnO_{4-\delta}$ at room temperature in the pristine state in air (g) and at 700°C in 5% H_2/Ar (h). The simulated hk0 and 0kl sections of the multiphase crystal consisting of the RP $n = 1$ and the perovskite structure (c,f). I4/mmm reflections are indexed in white, newly appeared perovskite reflections in green.

was heated in-situ to 700°C in vacuum. No silica shell was observed. However, in-situ 3DED data still only showed the partial transformation to perovskite, but no structural modulation corresponding to an oxygen-vacancy ordering.

In-situ high-resolution HAADF-STEM of one and the same $La_{0.5}Sr_{1.5}MnO_{4-\delta}$ crystal at room temperature and at 700°C in vacuum - without electron beam exposure in between - shows that it is the 2-3 nm amorphous surface layer that crystallizes into perovskite, whereas the bulk RP $n = 1$ phase remains unchanged (Figure 7a and 7b). Perovskite reflections were never observed at room temperature when using the illumination conditions as we use for 3DED (parallel beam with selected area aperture). So, the 3DED acquisition does not change the sample in a way that would influence the 3DED analysis. HAADF-STEM images of pristine $La_{0.25}Sr_{1.75}MnO_{4-\delta}$ do not show any amorphous layer or RP $n = 2$ defects (Figure 7c). There, the RP n=1 bulk phase always stretches until the very edge of the crystals. Nevertheless, in-situ 3DED in diluted hydrogen gas also evidences perovskite formation upon heating to 700°C (Figure 6h).

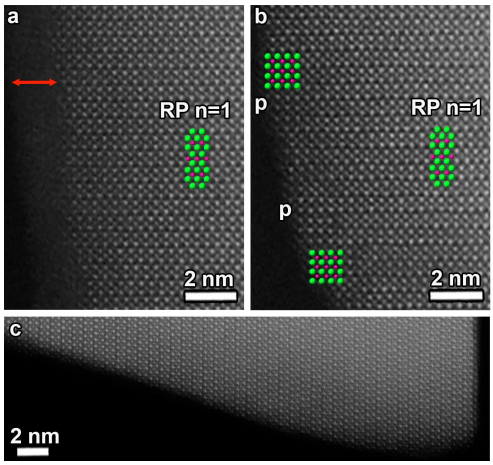

Figure 7: High-resolution HAADF-STEM images. (a): Pristine $La_{0.5}Sr_{1.5}MnO_{4-\delta}$ at room temperature. (b): The same crystal in-situ heated in vacuum at 700°C. In (b), perovskite domains (indicated as **p**) were created where the amorphous phase was previously present in (a) (red arrow). (c): Pristine $La_{0.25}Sr_{1.75}MnO_{4-\delta}$ where no amorphous phase or RP $n = 2$ layer defects are observed.

To determine the manganese valence state - and thus the effectivity of the reduction treatment - monochromated STEM electron energy-loss spectroscopy (mono STEM-EELS) was performed. In Figure 8, the L_2 and L_3 edges of the Mn fine structure are given for $La_{0.5}Sr_{1.5}MnO_{4-\delta}$ after in-situ heating in vacuum to 700°C (8a) and ex-situ heating in 5% H_2/Ar to 700°C (8b). In the in-situ gas heating experiments, the thickness of the double-chip Nano-reactor rendered the signal-to-noise ratio too low for a valid interpretation of the measurements (see Supplementary Information). Since the same structural transformation was observed in the 3DED data for in-situ heating in hydrogen as in vacuum, the mono STEM-EELS spectra for in-situ vacuum heated $La_{0.5}Sr_{1.5}MnO_{4-\delta}$ are used in this comparison. For this latter case (8a) the Mn L_3 edge is positioned at 643 eV at the outer surface, and gradually shifts to 644 eV at a depth of 60 nm, with an energy resolution of 0.5 eV. Comparing with MnO_2, Mn_2O_3 and MnO reference spectra,[12] this gives a mixture of Mn^{3+} and Mn^{4+}. However, the Mn L_3 edge of ex-situ annealed $La_{0.5}Sr_{1.5}MnO_{4-\delta}$ in a 5% hydrogen atmosphere is shifted to 641 eV. This indicates a lowering of the Mn valence to 2+ over the whole edge of the measured crystal (from the surface up to 50 nm into the bulk). Thus, the degree of reduction is much

lower for the in-situ vacuum heated material - where indeed no oxygen-vacancy ordering was observed with 3DED - as opposed to the ex-situ reduced sample.

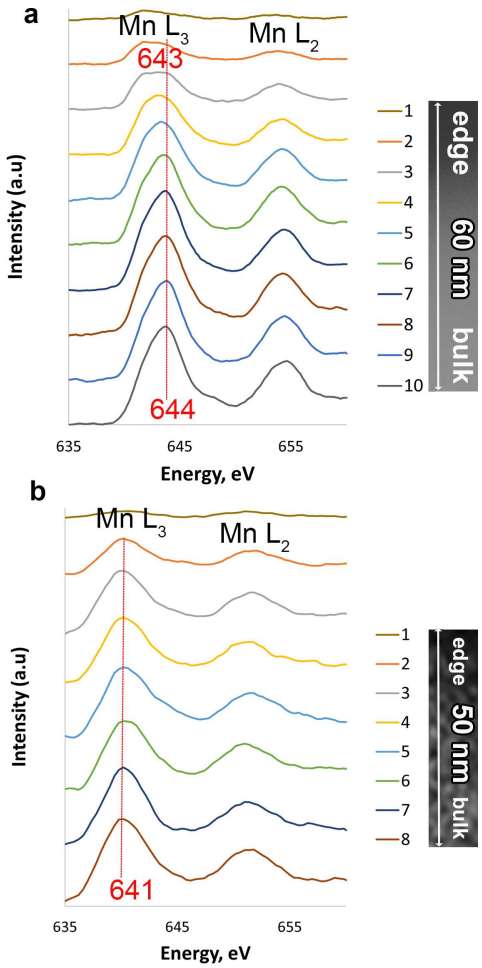

Figure 8: The L_2 and L_3 edge of the Mn fine structure from mono STEM-EELS of (a) $La_{0.5}Sr_{1.5}MnO_{4-\delta}$ after in-situ heating to 700°C in vacuum and (b) $La_{0.5}Sr_{1.5}MnO_{4-\delta}$ after ex-situ heating to 700°C in $5\%H_2$/Ar. In the former case, the L_3 peak shift indicates a mixture of Mn^{3+} and Mn^{4+}, while for the latter case Mn^{2+} is observed.

Discussion

Although according to literature[4] Ruddlesden-Popper manganites $La_xSr_{2-x}MnO_{4-\delta}$ with $0.25 \leq x \leq 0.6$ have the same I4/mmm structure, the $x = 0.5$ has a conductivity that breaks the trend of the other compositions. Especially in reducing SOFC anode conditions, its con-

ductivity is large in comparison to the compounds with a higher or lower lanthanum content. With ex-situ 3D electron diffraction (3DED) it was now possible to detect an incommensurate modulation in $La_{0.25}Sr_{1.75}MnO_{4-\delta}$ and $La_{0.5}Sr_{1.5}MnO_{4-\delta}$ due to ordering of the oxygen vacancies, when reduced in 5% H_2 at 700°C. While the resulting satellite reflections are very cleary visible in the reconstructed sections from 3DED (see Figure 2), the materials were previously reported to retain oxygen-vacancy disorder upon high-temperature reduction.[4]

The satellite reflections in modulated $La_{0.5}Sr_{1.5}MnO_{4-\delta}$ are much weaker than in modulated $La_{0.25}Sr_{1.75}MnO_{4-\delta}$ (Figure 2), suggesting that a smaller fraction of the overall crystal transforms into the modulated structure and thus the compound is less ordered. For both samples, 3DED data were repeated with a CCD as well as a direct electron detector under the same illumination conditions, giving systematically the same results. Goff et al.[13] showed that for yttria-stabilized zirconia, the ionic conductivity decreases with an increasing degree of order in the oxygen vacancies. Thus, the decreased oxygen-vacancy order might explain the much higher conductivity for $La_{0.5}Sr_{1.5}MnO_{4-\delta}$ at 800°C in diluted hydrogen gas (1.9 S cm $^{-1}$) with respect to compositions with higher and lower lanthanum content : (x = 0.25: 0.4 S cm^{-1}, x = 0.4: 0.5 S cm^{-1} and x= 0.6: 0.8 S cm^{-1}).

The x = 0.5 compound does not only break the conductivity trend with lanthanum doping in reducing conditions, but also in air (x = 0.25: 38.6 S cm^{-1}, x = 0.4: 33.6 S cm^{-1}, x = 0.5: 35.6 S cm^{-1} and x = 0.6: 28.8 S cm^{-1}).[4] This might be related to the abundant RP n = 2 layer defects in $La_{0.5}Sr_{1.5}MnO_{4-\delta}$, whereas they are absent in $La_{0.25}Sr_{1.75}MnO_{4-\delta}$. In-situ neutron diffraction studies of the vacancy localization and atomic displacement parameters of the $(La,Sr)_{n+1}(Co,Fe)_nO_{3n+1}$ Ruddlesden-Popper series suggest that oxygen transport pathways are rather located in the perovskite layers than the rock salt layers, causing the RP n = 1 structure to have to lowest oxygen mobility.[14] The presence of RP n = 2 defects could thus explain why $La_{0.5}Sr_{1.5}MnO_{4-\delta}$ breaks the downward trend in conductivity in air with

increasing x. However, the x = 0.25 composition still has a somewhat higher conductivity in the oxidized form than the x = 0.5 composition, because the effect of the defect structure does not exceed the influence of the doping concentration.

In pristine $La_{0.5}Sr_{1.5}MnO_{4-\delta}$, there is also an amorphous 2-3 nm La-rich surface layer. Previously Gonell et al.[15] already reported such an amorphous edge in $La_{0.5}Sr_{1.5}MnO_{4-\delta}$ formed during synthesis. Crystallization of an amorphous surface layer on a Ruddlesden-Popper manganite into a perovskite phase was observed earlier in RP $Pr_{0.5}Ca_{1.5}MnO_4$ by Mierwaldt et al.[16] after 7 minutes of electron beam exposure in 0.5 Pa H_2O, but the perovskite did not form in vacuum. This suggests that water vapour played an important role in the formation mechanism. However, for $La_{0.5}Sr_{1.5}MnO_{4-\delta}$ perovskite growth upon heating to 700°C was also observed in vacuum conditions with HAADF-STEM, and the addition of a molecular sieve to absorb water molecules (in-situ in a diluted hydrogen atmosphere, see Supporting Information for details) did not prevent perovskite formation either. No amorphous surface layer was observed in pristine $La_{0.25}Sr_{1.75}MnO_{4-\delta}$, although in-situ 3DED upon heating to 700°C in diluted hydrogen gas also showed perovskite growth. This suggests that in $La_{0.25}Sr_{1.75}MnO_{4-\delta}$ the perovskite forms from the layered RP $n = 1$ phase.

For both $La_{0.5}Sr_{1.5}MnO_{4-\delta}$ and $La_{0.25}Sr_{1.75}MnO_{4-\delta}$, the creation of perovskite domains can be explained by thermodynamics and their different elemental distribution at the surface. As shown in Figure 4, pristine $La_{0.5}Sr_{1.5}MnO_{4-\delta}$ has a lanthanum rich region at the surface compared to the bulk. But the La/Sr ratio has a crucial influence on the stability of phases in the La-Sr-Mn-O system. According to the calculated phase diagrams by Grundy et al.[17] using the compound energy formalism,[18] the stable coexisting phases at 800°C in reducing atmosphere ($\log(P(O_2) = 10^{-18}$) for $La_{0.5}Sr_{1.5}MnO_{4-\delta}$, $La_{0.25}Sr_{1.75}MnO_{4-\delta}$ and Sr_2MnO_4 are SrO, MnO and RP $n = 1$ $(La,Sr)_2MnO_4$. But when the lanthanum content locally gets doubled or more - as seen by EDX at the surface of $La_{0.5}Sr_{1.5}MnO_{4-\delta}$ in Figure 4 - also the

perovskite form (La,Sr)MnO_3 and higher order RP $n = 2$ $(La,Sr)_3MnO_7$ become stable. This is why no perovskite formation was observed in the case of Sr_2MnO_4. It must be noted that oxygen nonstoichiometry was not taken into account there, due to a lack of thermodynamic literature data for the relevant Ruddlesden-Popper phases.

Upon annealing in-situ in hydrogen gas, none of the samples displayed oxygen vacancy ordering, and EDX detected the formation of a shielding shell containing silicon. This layer around the crystals stems from the silicon nitride window of the heating chip on which the sample is drop casted for in-situ heating experiments. Wang et al.[19] already recorded the migration of SiO_2 from the support to diverse metal nanoparticles like Pt, Co, Ni, ... upon heating to 750°C in 10% H_2/Ar with in-situ high-resolution TEM images and EDX. Although the vacuum heating chips contain similar silicon nitride electron transparent windows as the gas heating chips, no such shell was detected by EDX upon heating in vacuum. However, as proven by mono STEM-EELS and in-situ 3DED, the high-temperature vacuum conditions (700°C-800°C) did not suffice to effectively reduce the x = 0.5 compound, although Sr_2MnO_4 was successfully reduced to $Sr_2MnO_{3.5}$ in vacuum at 550°C. Probably, the reaction with Si takes place in both experimental in-situ set-ups - gas and vacuum - but the silicon migration happens more slowly under vacuum conditions (10^{-7} mbar) than near-atmospheric pressure ($\pm$ 700 mbar). Because of the lower reduction temperature for the undoped x = 0 material compared to the other samples (550°C versus 700°C), oxygen vacancies could apparently still be created in Sr_2MnO_4 in vacuum before the silicon shell got too thick to prevent this.

The perovskite formation evidenced in our experiments, is not reversible upon either cooling or another heating cycle in oxidizing conditions. However, in the in-situ experiments, this could be caused by faster silica growth kinetics than the potential redox reactions involving the studied sample itself. Thus, the reversibility of the perovskite growth should still be examined in-situ without the presence of a SiO_2 layer, since it might have an effect on the

degradation of the materials as SOFC electrodes. A higher amount of perovskite blocks has a positive effect on oxygen mobility,[14] so this phenomenon might also contribute to the conductivity of the $La_xSr_{2-x}MnO_{4-\delta}$ series in a SOFC. Further research is required to determine the precise effect of surface perovskite formation during SOFC cycling on the cell's performance and lifetime.

Conclusion

Ruddlesden-Popper $La_xSr_{2-x}MnO_{4-\delta}$ solid oxide fuel cell (SOFC) electrode materials were studied for x = 0, 0.25 and 0.5 by different ex-situ and in-situ electron microscopy techniques, to examine the structural reasons behind the high conductivity for the x = 0.5 composition compared to compositions with a higher or lower La content, especially in reducing atmosphere as at the anode. 3D electron diffraction (3DED) discovered a structural transformation to an incommensurate 2D ($La_{0.25}Sr_{1.75}MnO_{4-\delta}$) and 1D ($La_{0.5}Sr_{1.5}MnO_{4-\delta}$) modulated structure upon annealing at 700°C in 5% H_2/Ar. This was previously undetected with powder X-ray and neutron diffraction. The systematically weaker satellites for x = 0.5 point to a lower degree of oxygen vacancy order, which can lead to a higher conductivity in reducing anode conditions.[13]

In pristine $La_{0.5}Sr_{1.5}MnO_{4-\delta}$, a 2-3 nm amorphous surface layer is systematically observed by high-resolution HAADF-STEM, as well as many higher-order RP $n = 2$ layer defects. The presence of these defects can also play a role in the enhanced conductivity, since they contain more perovskite blocks which are assumed to be the oxygen transport pathways,[14] and no such $n = 2$ defects are observed in $La_{0.25}Sr_{1.75}MnO_{4-\delta}$. Upon ex-situ or in-situ annealing in reducing environment at 700°C - diluted hydrogen gas or vacuum - also perovskite domains are created. In-situ high-resolution HAADF-STEM shows that for $La_{0.5}Sr_{1.5}MnO_{4-\delta}$, these domains originate from the crystallization of an originally amorphous surface layer. Such

perovskite formation at high temperature is important to take into account in conductivity and degradation studies for applications as an SOFC electrode. However, due to silicon migration of the dedicated heating chips, it was not possible to fully reduce the materials in-situ and monitor the transformation to the modulated structure by in-situ 3DED. The precise mechanism leading to the perovskite growth is not clear, but based on thermodynamics of the La-Sr-Mn-O system,[17] an important role is played by the La rich surface - as observed by EDX - and different structural phases are stable at the edge compared to the bulk structure in reducing environment. To completely understand this phenomenon, further research has to be performed, especially into the experimental set-up for in-situ electron microscopy, so that the reaction with silicon at high-temperatures can be avoided for this group of manganites and individual crystals can be tracked throughout the reaction in actual SOFC anode conditions.

Experimental

Synthesis

Sr_2MnO_4, $La_{0.25}Sr_{1.75}MnO_{4-\delta}$ and $La_{0.5}Sr_{1.5}MnO_{4-\delta}$ were synthesized by means of the solid state reaction. For Sr_2MnO_4, stoichiometric amounts of $SrCO_3$ (Sigma Aldrich 99.9%) and Mn_2O_3 (Sigma Aldrich 99.9%) powder were pressed into pellets of 1 cm in diameter using a hydraulic press. These pellets were heated for 18h hours at 1500°C in air. For $La_{0.25}Sr_{1.75}MnO_{4-\delta}$ and $La_{0.5}Sr_{1.5}MnO_{4-\delta}$, stoichiometric amounts of La_2O_3 (Alfa Aesar 99.9%), $SrCO_3$ (Sigma Aldrich 98%) and $MnCO_3$ (Sigma Aldrich 99.9%) were mixed and milled in an agate mortar for 2 hours. The resulting powders were uniaxially pressed into pellets of approximately 10 mm diameter. Then, the powders were calcined using three successive heating cycles at 1300 °C for 6h for x = 0.5. The x = 0.25 composition required three cycles at 1300°C for 6h, followed by 3 cycles at 1450°C for 6h and 1 cycle at 1450°C for 18h, performing intermediate grinding steps in all cases (note that pellets were always put

on a sacrificial bed of powder to avoid any possible diffusion between the alumina crucible and the pellet).

Powder X-ray Diffraction

After synthesis, the quality of the samples was checked with powder X-ray diffraction (XRD) using a Huber powder diffractometer with Cu-$K_{\alpha 1,2}$ equipped with a G670 Imaging Plate Guinier Camera. Powder XRD for ex-situ hydrogen annealed $La_{0.25}Sr_{1.75}MnO_{4-\delta}$ was performed with a high-flux Rigaku rotated Cu anode with Ni filter in Bragg-Brentano geometry. For as-synthesized Sr_2MnO_4, it was determined with XRD and Rietveld refinement, that apart from the intended β-Sr_2MnO_4 (I4/mmm, a = 3.78839(6) Å and c = 12.4955(3) Å) an admixture was created, consisting of the more stable α-phase, i.e. a mixture of SrO and $Sr_7Mn_4O_{15}$ ($P2_1/c$, a = 6.7931(4) Å, b = 9.6120(7) Å, c = 10.4259(5) Å, β= 92.053(5)°). But since 3DED series of each crystal were also acquired in the pristine state, it was possible to select only the β-phase for tracking during heating. Also the ex-situ annealed samples were examined with powder XRD (see Supplementary Information for details of the Le Bail fit). All reported cell parameters were determined from powder XRD. Le Bail fits and Rietveld refinement from powder XRD were performed using the software Jana2020.[20]

TEM Sample Preparation

After crushing the sample powder with mortar and pestel for about one minute, a suspension in ethanol was made and sonicated for about ten minutes in an ultrasonic bath, cooled with icepacks to prevent sample heating. This suspension was drop casted on a carbon coated Cu or Au grid, a DensSolutions EDX compatible Nano-Reactor consisting of an O-ring sealed top and bottom chip (gas heating) or a DensSolutions Nanochip for heating (in vacuum). Both types of chips contain electron transparent silicon nitride windows. After drop casting the sample, the (bottom) chip was plasma cleaned for 4 times 5 seconds in a 25% O_2/Ar mixture at 30% power to reduce contamination in the transmission electron microscope (TEM).

3D Electron Diffraction (3DED)

3DED data were acquired with a CCD camera (Gatan US1000XP) in a stepwise manner with tilt steps of 0.5°, or - for the dynamical refinement of ex-situ reduced $La_{0.25}Sr_{1.75}MnO_{4-\delta}$ - with a direct electron detector (ASI CheeTah) with a 1° tilt step and 1° precession semi-angle. The total angular tilting range was about -20° to 20° for the DensSolutions Climate holder (gas heating), -30° to 30° for the DensSolutions single tilt Wildfire heating holder (vacuum heating) and -70° to 70° for the Fischione tomo holder (ex-situ 3DED). All 3DED experiments were recorded in TEM mode at a Thermo Fisher Tecnai G2 or Titan^3 at 200 kV and 300 kV respectively. Either a 200 nm selected area aperture or a 300-600 nm parallel beam was used, depending on the crystal size. The acquisition was done manually (total acquisition about 30'-45') or semi-automatically, using either an in-house written Digital Micrograph script that allows intermediate manual crystal position adjustment (total acquisition 15'-20'), or the fast-ADT software[21] with prior crystal tracking in image mode (total acquisition about 10'). If specified explicitly, the data were acquired while precessing the beam at 150 Hz with a 1° semi-angle, using the Nanomegas system. After data acquisition, all diffraction patterns were processed with the PETS2 software[22] to reconstruct the three-dimensional reciprocal space and make two-dimensional reconstructions of selected crystallographic sections. Dynamical refinement was done with Jana2020 including Dyngo.[20]

In Situ Electron Diffraction during a Gas-Solid Reaction

In-situ gas experiments were performed using the Climate single-tilt holder and an EDX compatible Nano-Reactor from DensSolutions, creating a 10 μm thick sealed volume. Before heating in gas, 3DED series of the pristine sample were taken at room temperature in vacuum (10^{-7} mbar), in air or nitrogen gas (700 mbar). As a reducing agent, H_2 was diluted with He or Ar (concentration explicitly mentioned). Before introducing the gases, each gas line was vacuum pumped 1 to 3 times in order to eliminate as much remaining oxygen as possible. Inside the sealed Nano-Reactor, the gas pressure was 700 mbar, and the gas flow varied

between 0.1 ml (pure argon) and 0.5 ml (pure helium) per minute. Detailed descriptions of all in-situ gas heating experiments are provided in the supplementary information.

High-resolution HAADF-STEM

High-resolution high-angle annular dark field scanning transmission electron microscopy (HAADF-STEM) images were acquired at 300 kV with a Thermo Fisher Titan^3 instrument. For the in-situ HAADF-STEM experiments in vacuum, the double tilt Wildfire heating holder from DensSolutions was used, and images were taken at room temperature and at 700°C.

(Monochromated STEM) Eelectron Energy-Loss Spectroscopy (EELS)

(Monochromated STEM) electron energy-loss spectroscopy (EELS) experiments were performed at a Thermo Fisher Titan^3 at 300 kV with a Quantum 966 or Enfinium Gatan Image Filter and a US1000XP CCD camera. If the monochromator was used, it was excited to 0.7. For energy calibration, dual EELS was performed to include the zero-loss peak.

Energy-Dispersive X-ray Spectroscopy (EDX)

Energy-Dispersive X-ray Spectroscopy (EDX) mapping was performed in STEM mode at 300 kV at a Thermo Fisher Titan^3 instrument or at 200 kV at a Tecnai G2 with a Super X detector. All spectra were processed using the Esprit software. The additional EDX maps in the Supporting Information were taken at a Thermo Fisher Quanta 250 FEG Scanning Electron Microscope at 20 kV, and processed using the Aztec software.

Supporting Information Available

PDF file containing:

- powder XRD data and Le Bail fit parameters

- ex-situ reduced, modulated $La_{0.25}Sr_{1.75}MnO_{4-\delta}$:
  - dynamical refinement parameters from 3DED
  - Rietveld refinement parameters from powder XRD
  - EDX maps and quantified data
- experimental details for in-situ 3DED
- in-situ mono STEM-EELS details

Acknowledgement

The authors thank Michael Hayward for the synthesis of $La_{0.75}Sr_{1.25}MnO_{4-\delta}$ and $LaSrMnO_{4-\delta}$, and for his help regarding the use of zirconium for oxygen molecule absorption while heating in-situ, Olesia Karakulina for providing the smoothing script for EELS visualisation and Nicolas Gauquelin for his help with the mono STEM EELS acquisition. This research was financially supported by FWO I003218N, University of Antwerp BOF TOP 38689 and the European Commission NanED Grant number 956099.

References

(1) Cooper, S. J.; Brandon, N. P. *An Introduction to Solid Oxide Fuel Cell Materials, Technology and Applications*; Elsevier Inc., 2017.

(2) Sandoval, M. V. *Etude de manganites Ruddlesden-Popper RExA2xMnO4 (Re: La, Nd; A: Sr, Ca) en vue de leur application en tant que materiaux d'electrode de pile a combustile a oxide solide (SOFC)*; PdH Thesis: Universite de Lille, Universidad industrial de Santander, 2017.

(3) Munnings, C. N.; Skinner, S. J.; Amow, G.; Whitfield, P. S.; Davidson, I. J. Structure, stability and electrical properties of the La(2-x)SrxMnO4 solid solution series. *Solid State Ionics* **2006**, *177*, 1849–1853.

(4) Sandoval, M. V.; Pirovano, C.; Capoen, E.; Jooris, R.; Porcher, F.; Roussel, P.; Gauthier, G. H. In depth study of the RuddlesdenPopper LaxSr2-xMnO4 family as possible electrode materials for symmetrical SOFC. *International Journal of Hydrogen Energy* **2017**, *42*, 21930–21943.

(5) Batuk, M.; Vandemeulebroucke, D.; Ceretti, M.; Paulus, W.; Hadermann, J. Topotactic redox cycling in SrFeO2.5 explored by 3D electron diffraction in different gas atmospheres. *Journal of Materials Chemistry A* **2022**, *11*, 213–220.

(6) Kruidhof, H.; Bouwmeester, H.; van Doorn, R.; Burggraaf, A. Influence of order disorder transitions on oxygen permeability through selected nonstoichiometric perovskite-type oxides. *Solid State Ionics* **1993**, 1816–1822.

(7) Hadermann, J.; Pérez, O.; Créon, N.; Michel, C.; Hervieu, M. The (3 + 2)D structure of oxygen deficient LaSrCuO3.52. *Journal of Materials Chemistry* **2007**, 2344–2350.

(8) Klar, P.; Krysiak, Y.; Xu, H.; Steciuk, G.; Cho, J.; Zou, X.; Palatinus, L. Accurate Structure Models and Absolute Configuration Determination using Dynamical Effects in Continuous-Rotation 3D Electron Diffraction Data. *Nature Chemistry* **2023**, 848–855.

(9) Gillie, L.; Wright, A.; Hadermann, J.; Tendeloo, G. V.; Greaves, C. Synthesis and characterization of the reduced single-layer manganite Sr2MnO3.5+x. *Journal of Solid State Chemistry* **2002**, *167*, 145–151.

(10) Broux, T.; Bahout, M.; Hernandez, O.; Tonus, F.; Paofai, S.; Hansen, T.; Greaves, C. Reduction of Sr2MnO4 investigated by high temperature in situ neutron powder diffraction under hydrogen flow. *Inorganic Chemistry* **2013**, *52*, 1009–1017.

(11) Vatanparast, M.; Egoavil, R.; Renaas, T.; Verbeeck, J.; Holmestad, R.; Vullum, P. Bandgap measurement of high refractive index materials by off-axis EELS. *Ultramicroscopy* **2017**, 92–98.

(12) Tan, H.; Verbeeck, J.; Tendeloo, G. V. Oxidation state and chemical shift investigation in transition metal oxides by EELS. *Ultramicroscopy* **2012**, 24–33.

(13) Goff, J.; Hayes, W.; Hull, S.; Hutchings, M.; Clausen, K. Defect structure of yttria-stabilized zirconia and its influence on the ionic conductivity at elevated temperatures. *Physical Review B* **1999**, *59*, 14202–14219.

(14) Tomkiewicz, A.; Tamimi, M.; Huq, A.; McIntosh, S. Oxygen transport pathways in Ruddlesden-Popper structured oxides revealed via in-situ neutron diffraction. *Journal of Materials Chemistry A* **2015**, 21864–21874.

(15) Gonell, F.; Sanchez-Sanchez, C. M.; Vivier, V.; Méthivier, C.; Laberty-Robert, C.; Porteheat, D. Structure Activity Relationship in Manganese Perovskite Oxide Nanocrystals from Molten Salts for Efficient Oxygen Reduction Reaction Electrocatalysis. *Chemistry of Materials* **2020**, 4241–4247.

(16) Mierwaldt, D.; Roddatis, V.; Christian, J. Environmental TEM Investigation of Electrochemical Stability of Perovskite and Ruddlesden–Popper Type Manganite Oxygen Evolution Catalysts. *Advanced Sustainable Systems* **2017**, *1*, 1700109.

(17) Grundy, A.; Hallstedt, B.; Gauckler, L. Assessment of the La-Sr-Mn-O System. *Computer Coupling of Phase Diagrams and Thermochemistry* **2004**, 191–201.

(18) Hillert, M. The compound energy formalism. *Journal of Alloys and Compounds* **2001**, 161–176.

(19) Wang, L.; Zhang, L.; Zhang, L.; Yang, F. Direct Environmental TEM observation of sil-

icon diffusion-induced strong metal-silica interaction for boosting CO2 hydrogenation. *Nano Research* **2022**, *2*, 2209–2217.

(20) Petricek, V. Jana2020 software, http://jana.fzu.cz, version of April 6, 2023.

(21) Plana-Ruiz, S.; Krysiak, Y.; Portillo, J.; Alig, E.; Estradé, S.; Peiró, F.; Kolb, U. Fast-ADT: A fast and automated electron diffraction tomography setup for structure determination and refinement. *Ultramicroscopy* **2020**, *211*, 112951.

(22) Palatinus, L., PETS2 software, http://pets.fzu.cz/, version of February 2, 2023.

TOC Graphic

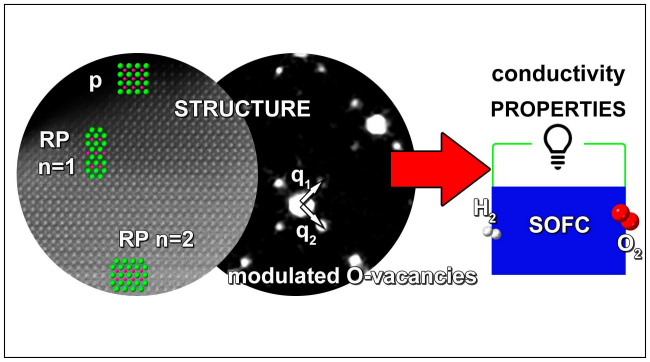
p
STRUCTURE
RP
n=1
RP n=2
q1
q2
modulated O-vacancies
conductivity
PROPERTIES
H2
SOFC
O2

Supporting Information

Incommensurate Modulations and Perovskite Growth in $La_xSr_{2-x}MnO_{4-\delta}$ Affecting Solid Oxide Fuel Cell Conductivity

Daphne Vandemeulebroucke*[1], Maria Batuk[1], Amirhossein Hajizadeh[1], Myriam Wastiaux[2], Pascal Roussel[2] and Joke Hadermann[1]

[1]EMAT, University of Antwerp, Groenenborgerlaan 171, 2020 Antwerpen, Belgium
[2]UCCS, University of Lille, CNRS UMR8181, Avenue Mendeleiev, 59655 Villeneuve d'Ascq Cedex, France

*daphne.vandemeulebroucke@uantwerpen.be

Contents

1. Powder XRD

1.1. $La_{0.25}Sr_{1.75}MnO_{4-\delta}$

1.1.1. As-synthesized

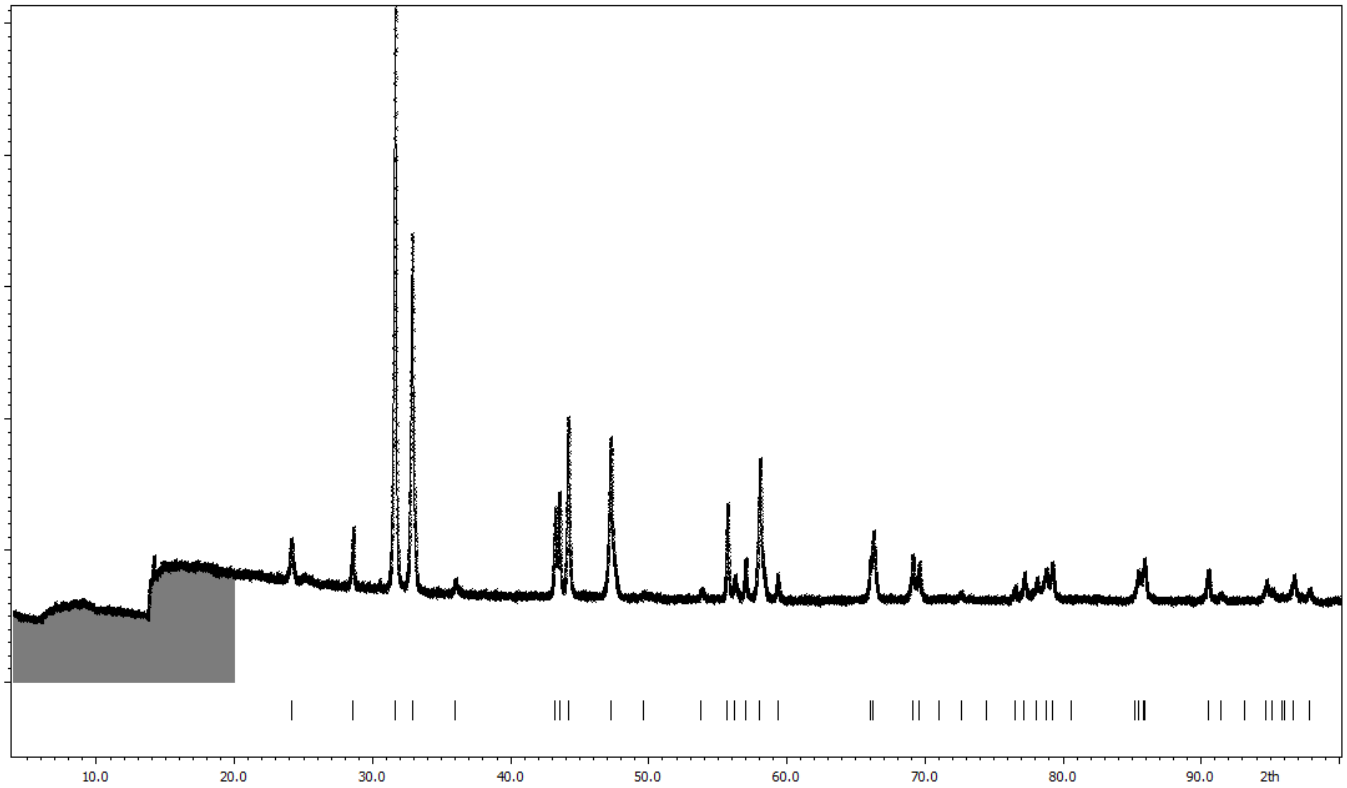

1.1.2. Ex-situ annealed at 550°C in N2 and at 700°C in 5% H2/Ar

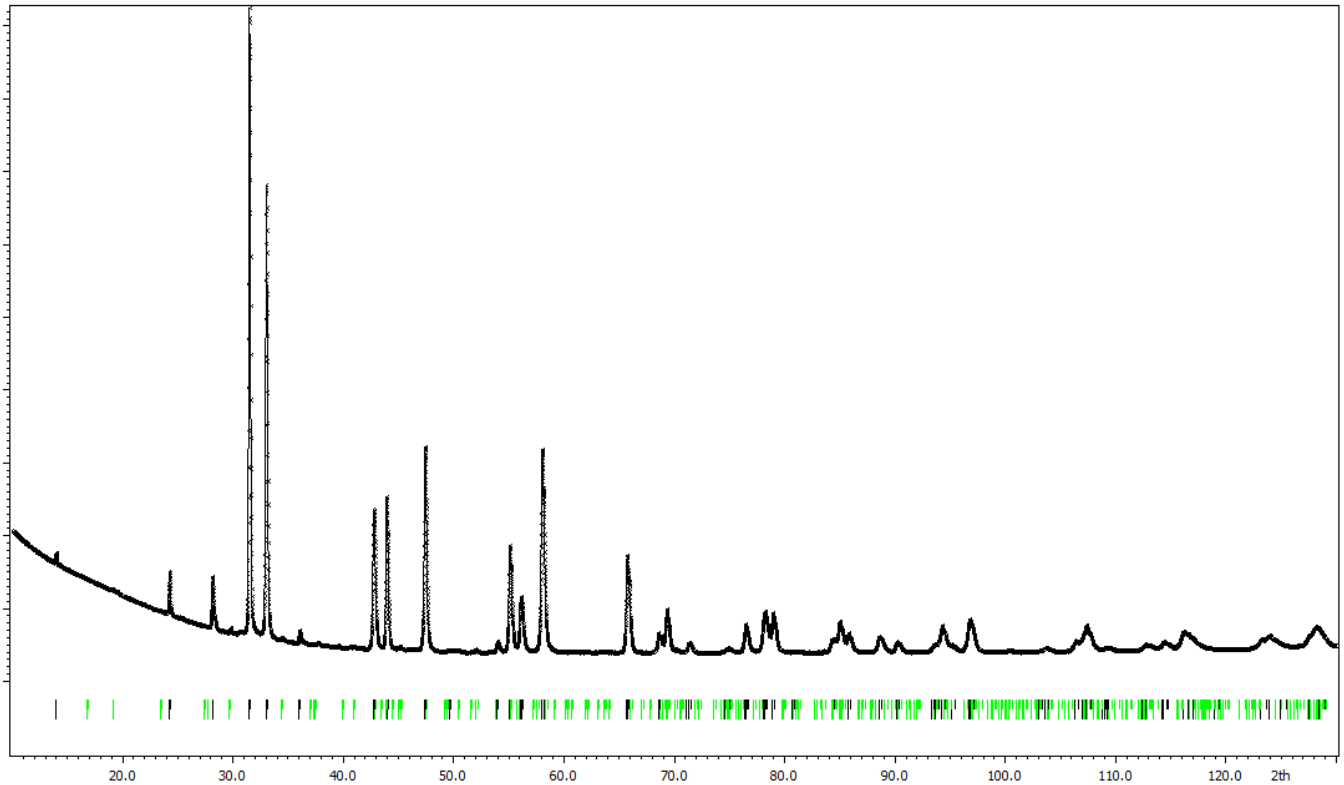

1.2. $La_{0.5}Sr_{1.5}MnO_{4-\delta}$

1.2.1. As-synthesized

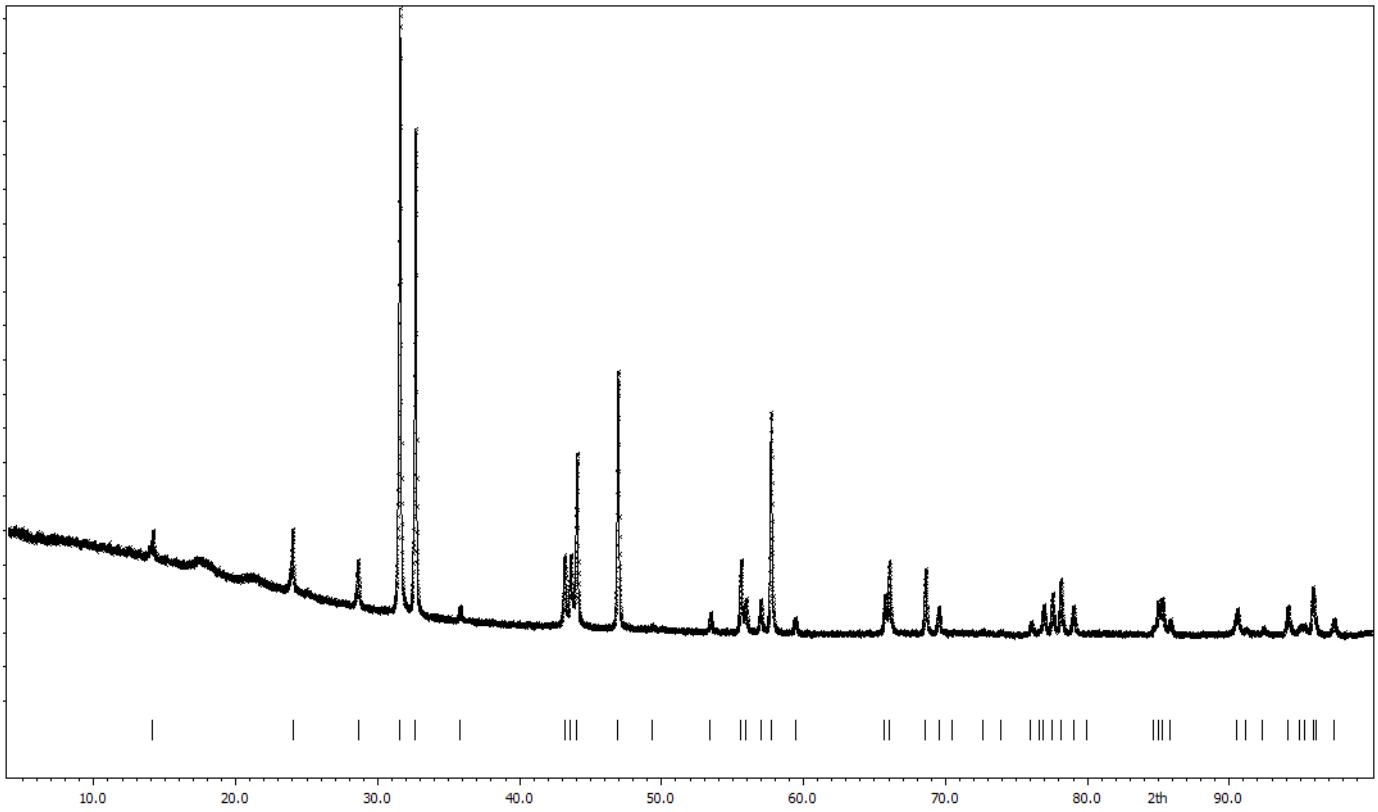

1.2.2. Ex-situ annealed at 550°C in N_2 and at 700°C in 5% H_2/Ar

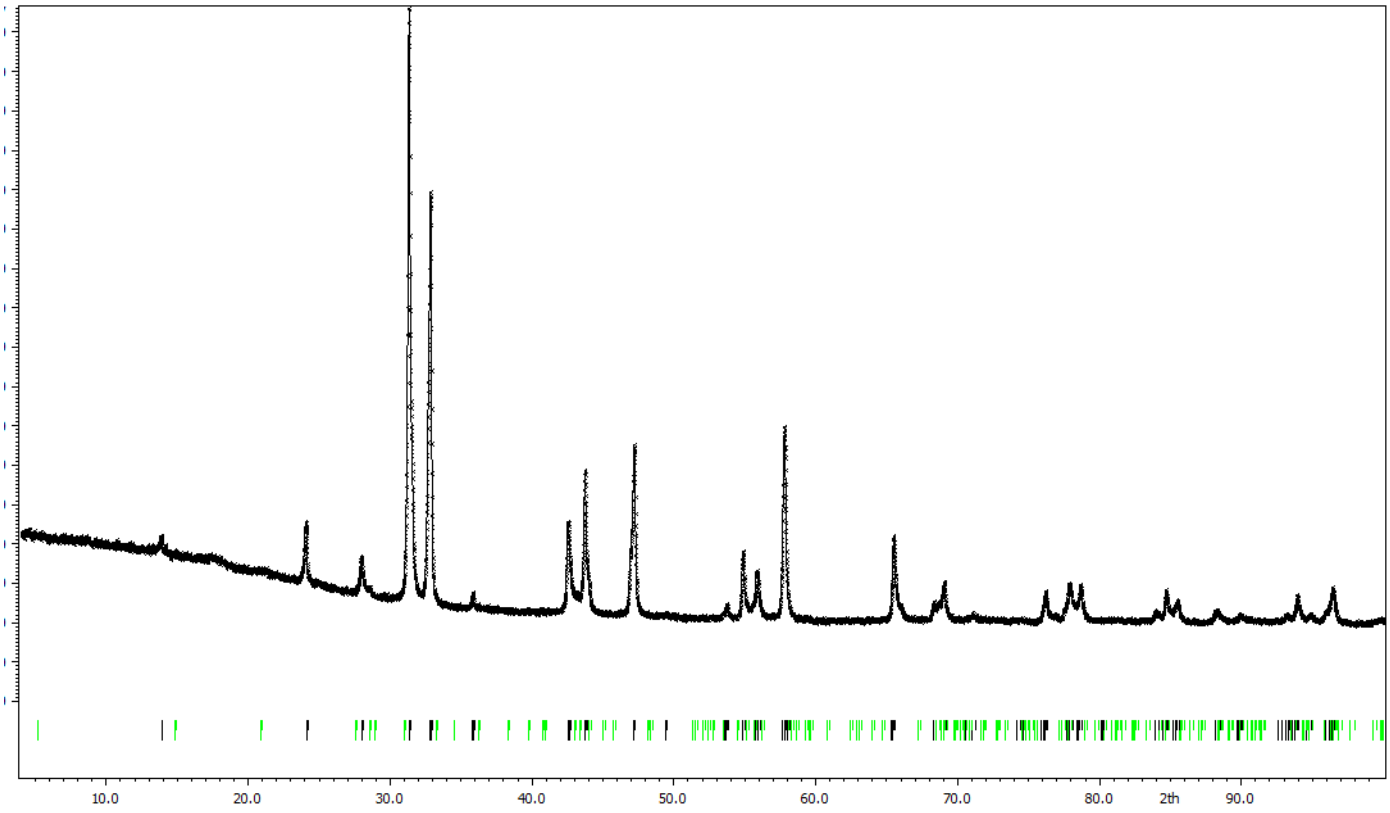

1.3. $Sr_2MnO_{4-\delta}$

1.3.1. As-synthesized

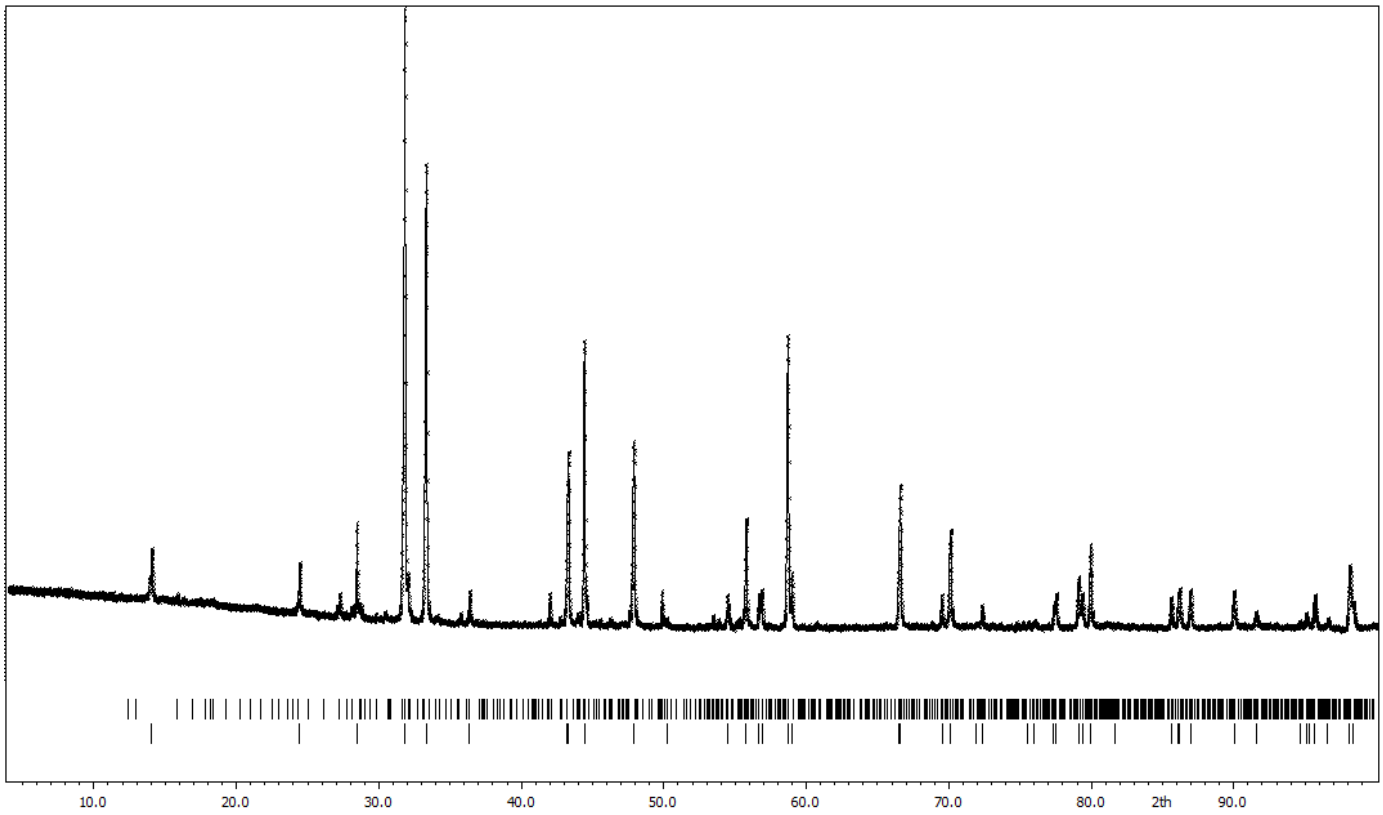

1.3.2. Ex-situ annealed at 550°C in N_2

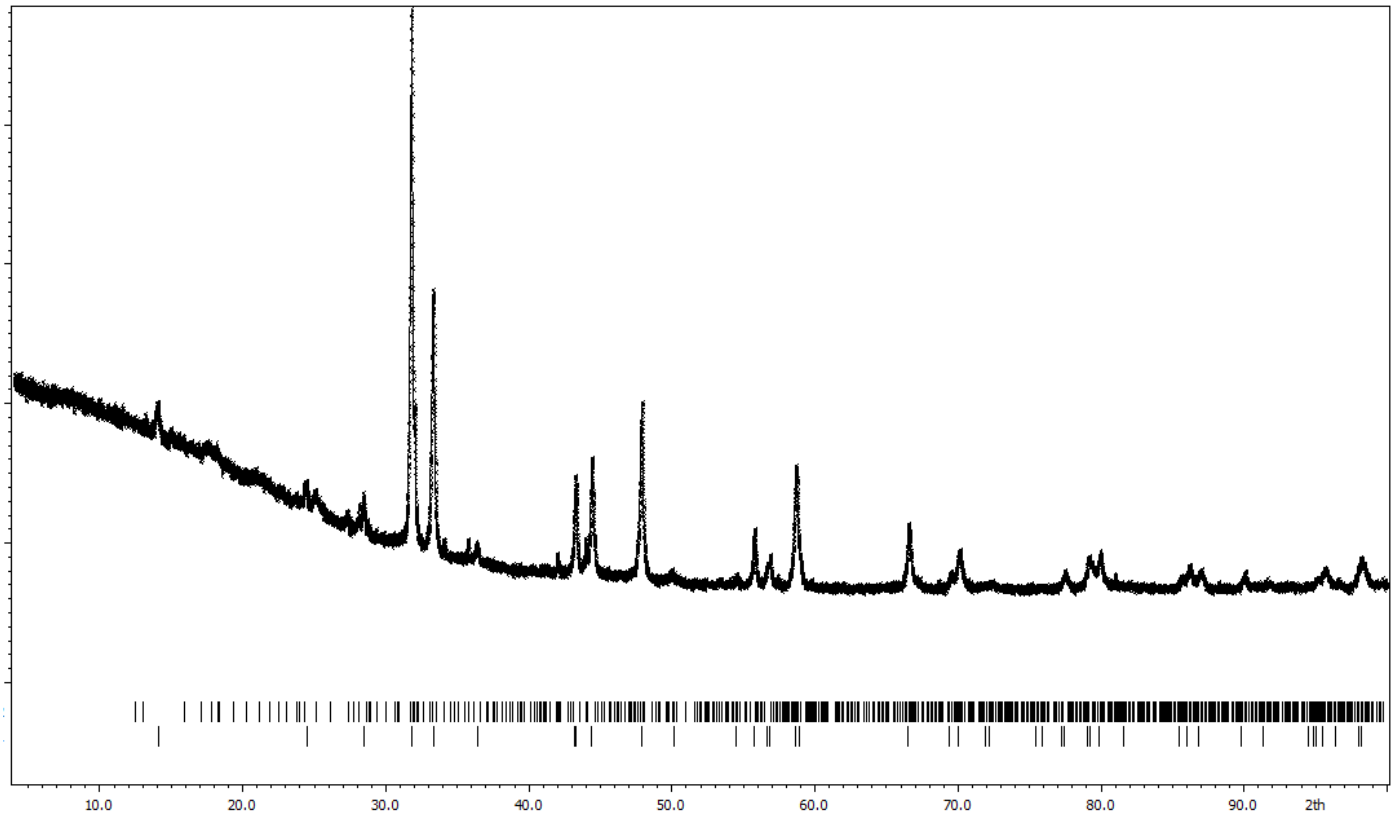

1.3.3. Ex-situ annealed at 550°C in N_2 and at 700°C in 5% H_2/Ar

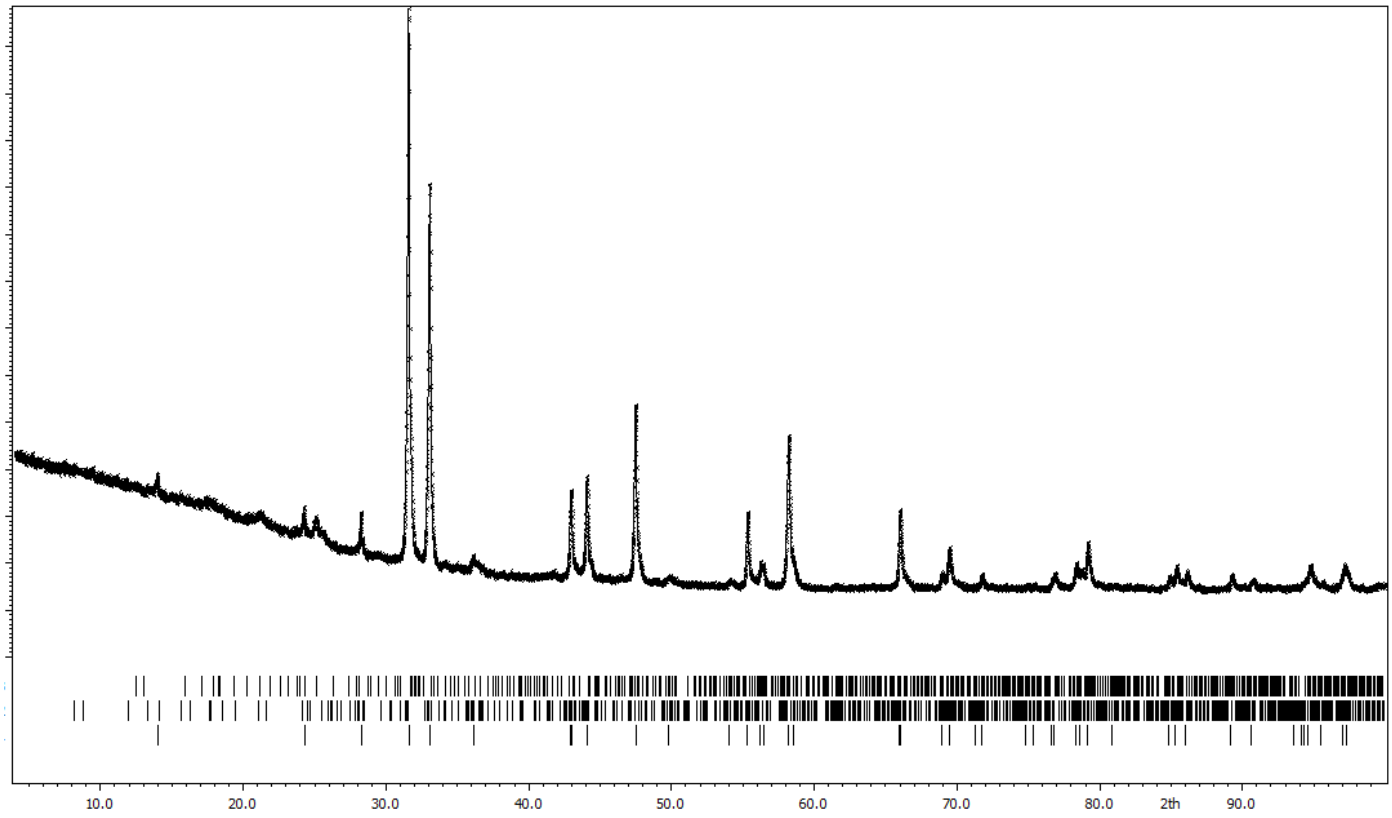

1.4. $La_{0.75}Sr_{1.25}MnO_{4-\delta}$

1.4.1. As-synthesized

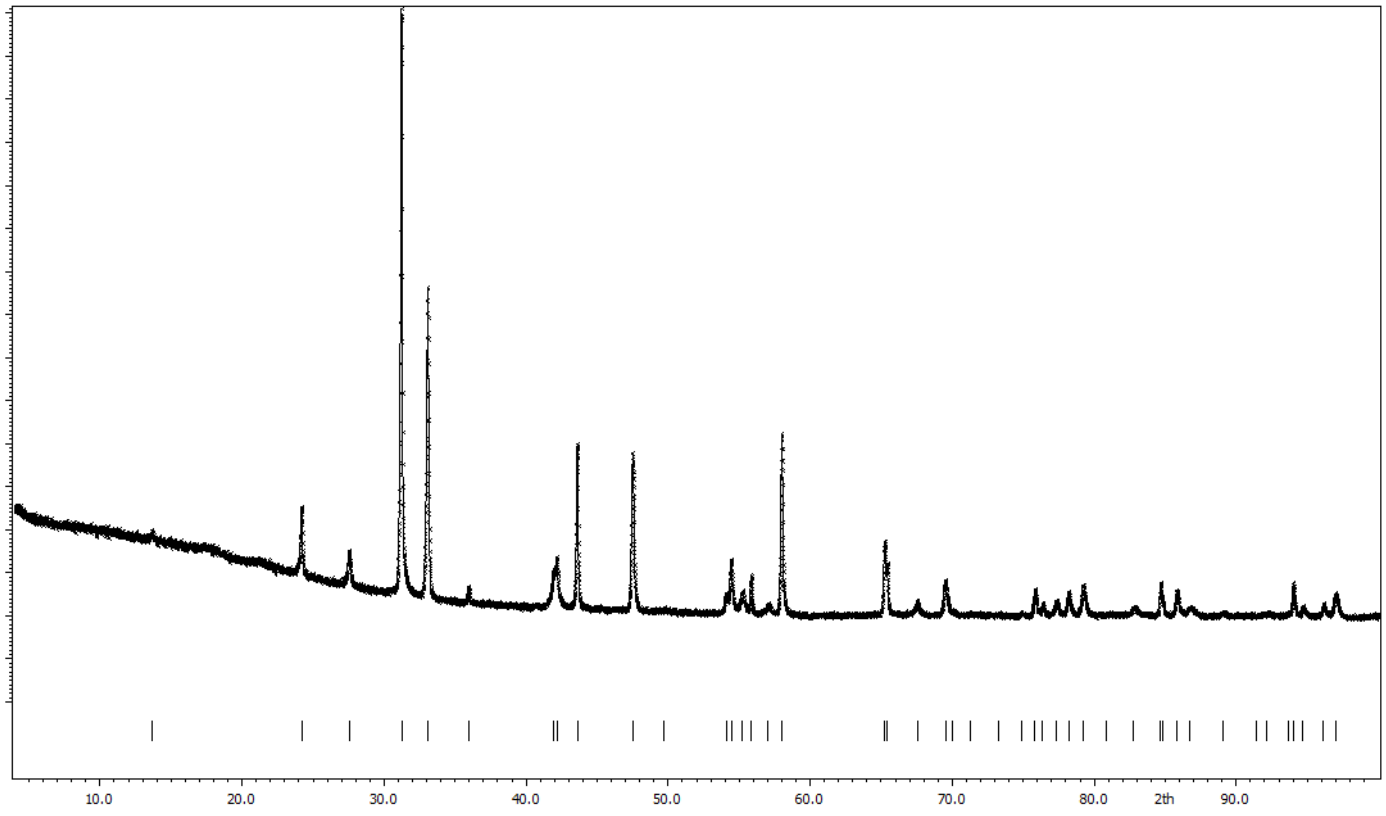

1.4.2. Ex-situ annealed at 550°C in N_2 and at 700°C in 5% H_2/Ar

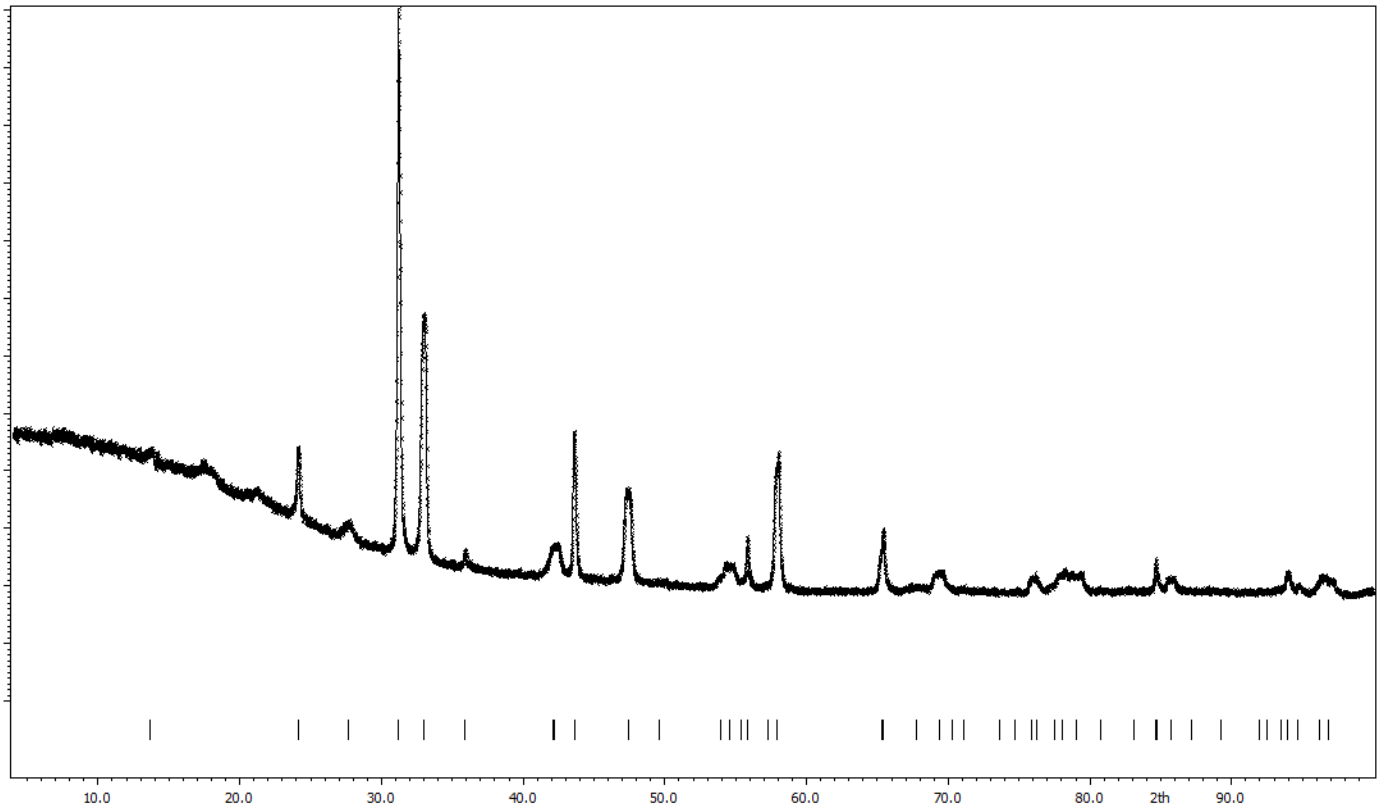

1.5. $LaSrMnO_{4-\delta}$

1.5.1. As-synthesized

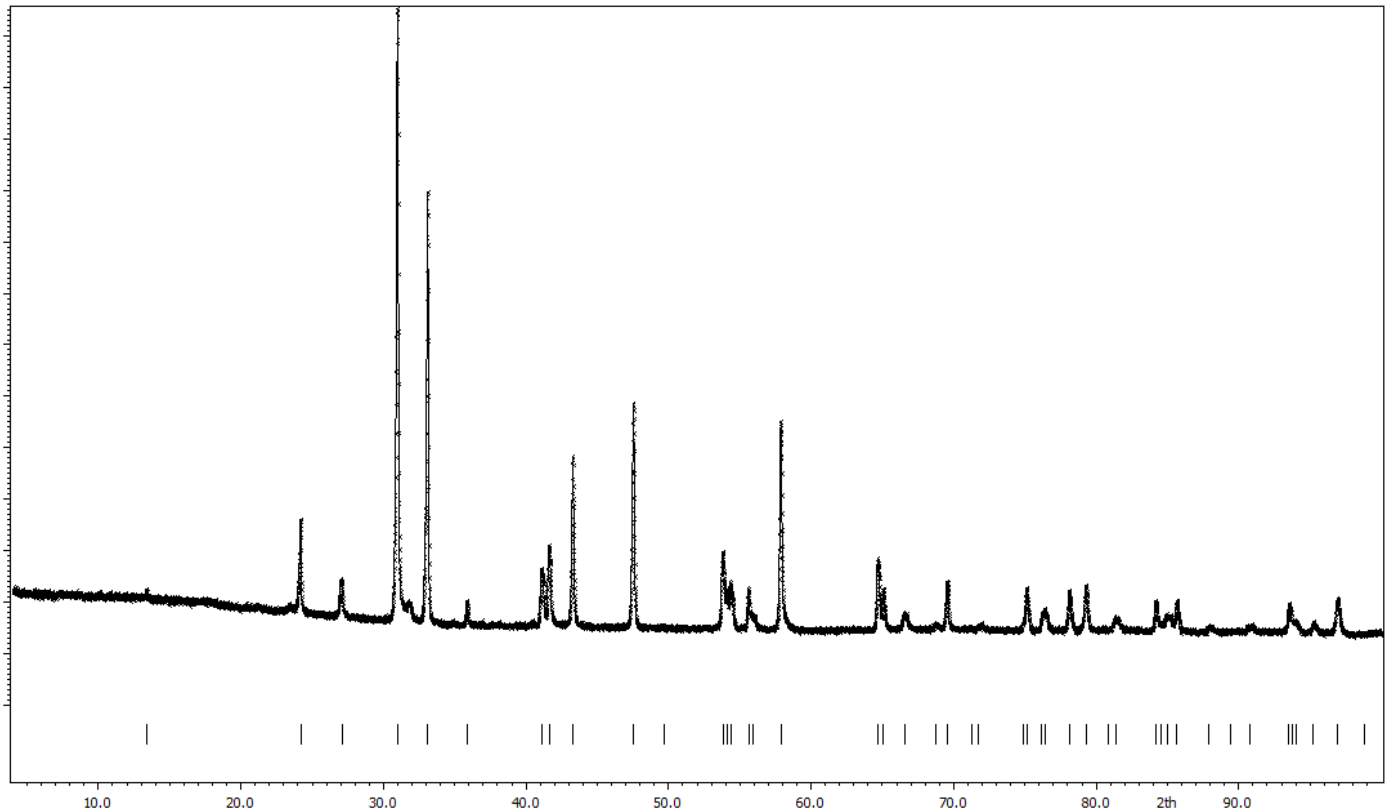

1.5.2. Ex-situ annealed at 550°C in N_2 and at 700°C in 5% H_2/Ar

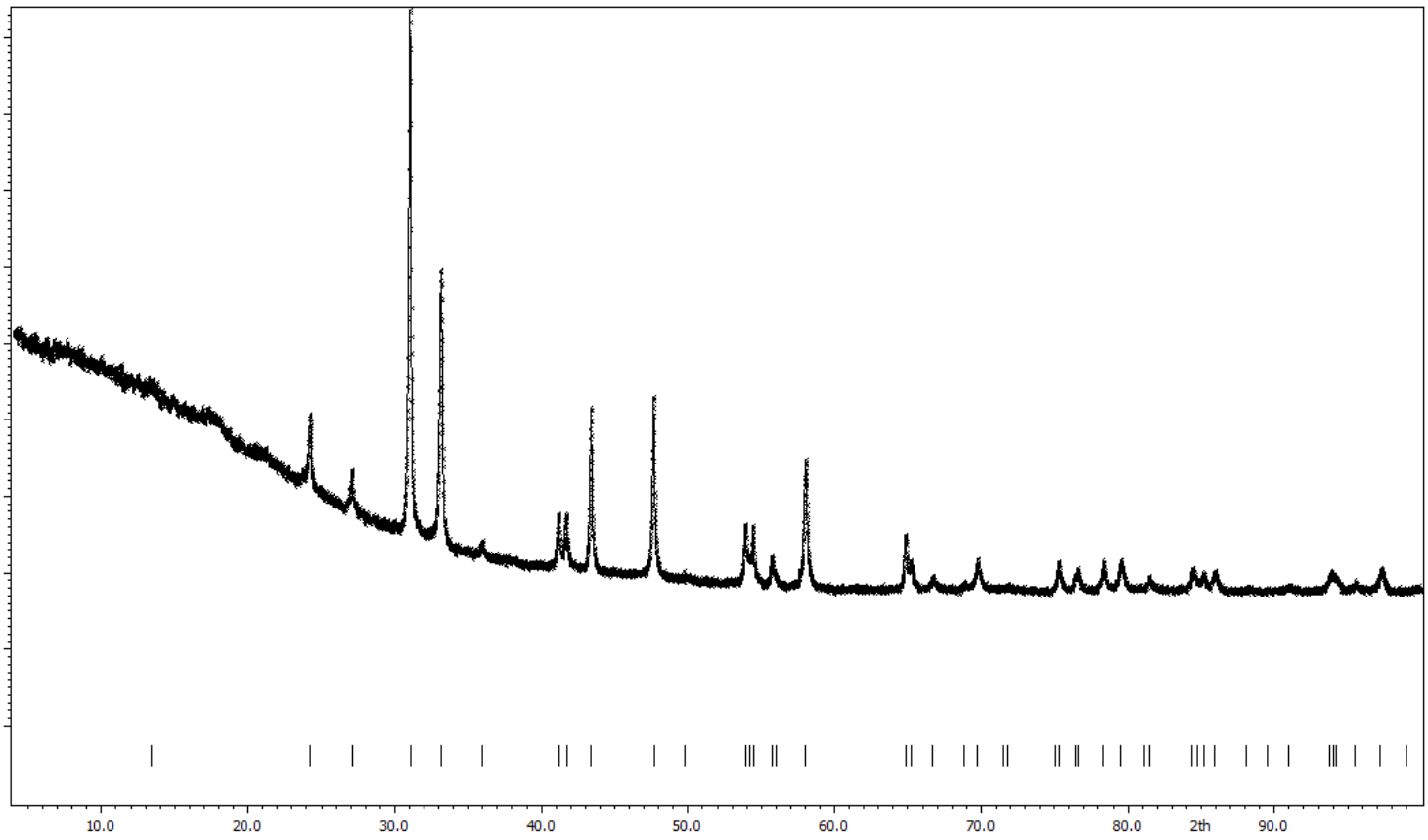

2. Cell parameters from powder XRD

2.1. $La_{0.25}Sr_{1.75}MnO_{4-\delta}$ and $La_{0.5}Sr_{1.5}MnO_{4-\delta}$

Table 1				
	$La_{0.25}Sr_{1.75}MnO_{4-\delta}$ pristine	**$La_{0.25}Sr_{1.75}MnO_{4-\delta}$ annealed in 5%H_2/Ar**	**$La_{0.5}Sr_{1.5}MnO_{4-\delta}$ pristine**	**$La_{0.5}Sr_{1.5}MnO_{4-\delta}$ annealed in 5%H_2/Ar**
a (Å)	3.8324(3)	3.8324(7)	3.86007(7)	5.4537(6)
b (Å)				12.711(2)
c (Å)	12.422(1)	12.6725(5)	12.4135(5)	5.4403(5)
q vectors		0.2848(1) (a* + b*) 0.2848(1) (a* - b*)		0.318(2)c*
GOF	0.66	3.92	1.02	1.41
R_p	2.27	1.39	1.83	2.13
wR_p	3.50	2.16	2.78	3.85

2.2. $Sr_2MnO_{4-\delta}$

Table 2			
	$Sr_2MnO_{4-\delta}$	$Sr_2MnO_{4-\delta}$ annealed in N_2	$Sr_2MnO_{4-\delta}$ annealed in 5% H_2/Ar
phase 1			
a (Å)	3.78839(6)	3.79577(8)	3.8247(1)
c (Å)	12.4955(3)	12.5338(4)	12.6039(9)
phase 2			
a (Å)	6.7931(4)	6.8102(4)	6.773(3)
b (Å)	9.6120(7)	9.6741(5)	9.682(4)
c (Å)	10.4258(5)	10.3877(6)	10.382(5)
β (°)	92.053(5)	91.981(4)	91.97(3)
phase 3			
a (Å)			6.82(1)
b (Å)			10.89(1)
c (Å)			10.95(2)
β (°)			113.5(2)
GOF	1.11	0.48	1.16
R_p	2.39	1.62	2.30
wR_p	3.83	2.14	3.54

2.3. $La_{0.75}Sr_{1.25}MnO_{4-\delta}$ and $LaSrMnO_{4-\delta}$

Table 3				
	$La_{0.75}Sr_{1.25}MnO_{4-\delta}$ pristine	$La_{0.75}Sr_{1.25}MnO_{4-\delta}$ annealed in 5%H_2/Ar	$LaSrMnO_{4-\delta}$ pristine	$LaSrMnO_{4-\delta}$ annealed in 5%H_2/Ar
a (Å)	3.81784(4)	3.8224(2)	3.81624(2)	3.80592(7)
c (Å)	12.9040(3)	12.84(1)	13.1324(2)	13.1152(4)
GOF	0.80	1.18	0.88	0.61
R_p	1.58	2.05	2.02	1.34
wR_p	2.22	3.26	3.00	1.71

GOF stands for the "goodness of fit" and the profile R-factors stated in these tables are [1]:

$$R_p = \frac{\sum_i |y_i(obs) - y_i(calc)|}{y_i(obs)} \cdot 100$$

$$wR_p = \sqrt{\frac{\sum_i w_i (y_i(obs) - y_i(calc))^2}{\sum_i w_i y_i(obs)^2}} \cdot 100$$

with weights from the standard uncertainties of the profile intensities:

$$w_i = \frac{1}{\sigma^2(y_i(obs))}$$

3. EDX of hydrogen annealed $La_{0.25}Sr_{1.75}MnO_{4-\delta}$

Energy-dispersive X-ray analysis (EDX) of in diluted hydrogen annealed $La_{0.25}Sr_{1.75}MnO_{4-\delta}$ shows that the elemental composition of the sample is not homogeneous. The quantified data largely fall into three subsets (see Table 4, grey-orange-white). However, about half of the examined particles possesses a composition close to the theoretical atomic percentages (La: 3.57%, Sr: 25%, Mn: 14.29%). Since the La and Sr occupancies could not be refined from either 3DED or powder XRD data, those were fixed to the theoretical values in the refinements of which the details are listed in the next section.

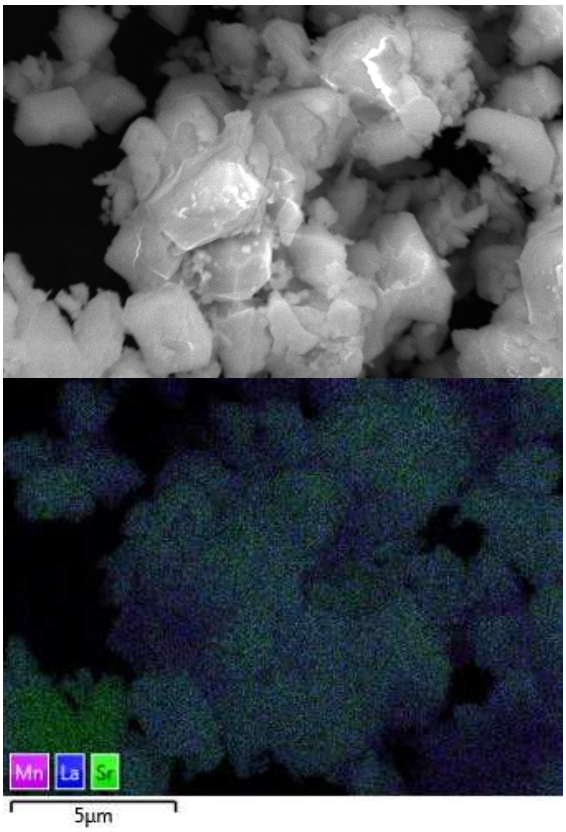

Figure S1: Scanning electron microscope image and EDX map of hydrogen annealed $La_{0.25}Sr_{1.75}MnO_{4-\delta}$, illustrating the elemental inhomogeneity. Pink: Mn; blue: La; green: Sr.

Table 4: Atomic percentages for La, Sr and Mn from EDX of 26 particle areas. The data can be divided into three groups, from which the majority possesses the theoretical composition.

Table 4			
No.	La (at%)	Sr (at. %)	Mn (at. %)
1	3.1	21.8	12.0
2	3.7	24.8	16.3
3	3.0	22.0	11.8
4	3.2	21.4	12.5
5	3.4	226.	12.8
6	3.1	24.4	12.3
7	3.8	23.8	13.7
8	4.0	23.0	14.8
9	3.0	225.	12.8
10	3.6	23.4	14.3
11	3.6	23.0	13.1
12	3.0	21.5	11.6
13	9.8	25.8	39.1
14	8.6	27.0	41.1
15	7.5	22.8	32.1
16	8.9	23.8	37.2
17	8.0	29.0	34.2
18	9.5	22.0	41.0
19	8.8	25.2	37.2
20	7.8	28.9	36.2
21	8.1	27.5	37.7
22	7.6	26.1	29.5
23	8.4	21.7	33.4
24	5.0	27.6	20.9
25	5.8	24.9	24.5
26	5.3	28.8	23.3

4. Structural refinements for hydrogen annealed $La_{0.25}Sr_{1.75}MnO_{4-\delta}$

Refined parameters for ex-situ reduced $La_{0.25}Sr_{1.75}MnO_{4-\delta}$ are listed below, both for the dynamical refinement from precession 3DED as for the kinematical Rietveld refinement from powder XRD. La and Sr occupancies were kept fixed, as discussed in the previous section. Where up to 4 modulation waves were used for the 3DED refinement, only 2 of them were taken in the XRD refinement, since only satellite reflections with indices l,m = 0,1 or 1,0 are experimentally visible there. No occupancy modulations were used for Mn in the 3DED refinement, since this leads to non-physical values.

The discrepancy between both methods can be partially explained by the higher sensitivity of electrons versus X-ray, leading to the observation of more satellites by the latter technique (also the mixed indices l,m = 1,1 and even up to 2). Furthermore, as shown by the EDX maps in the previous section, the sample is inhomogeneous in its elemental composition. This can also cause structural variety between individual crystals, over which powder XRD will be averaged, whereas the 3DED data was acquired from one single crystal.

4.1. Dynamical refinement from precession 3DED

$La_{0.25}Sr_{1.75}MnO_{4-\delta}$ annealed in 5%H_2/Ar	
La/Sr (x,y,z)	**0, 0, 0.3533(2)**
La/Sr ($s_{1/2}$)	0.0197(3)
La/Sr (ys_3, xs_4)	0.0030(3)
La/Sr (zc_3)	0.00359(9)
La/Sr (U_{11}, U_{33})	0.0320(8), 0.014(1)
Mn (x,y,z)	**0, 0, 0**
Mn ($s_{1/2}$, ys_3)	0.0033(2), -0.0196(4)
Mn (U_{iso})	0.001(1)
O1 (x,y,z)	**0, 0, 0.1586(5)**
O1 (U_{iso})	0.041(2)
O1 ($s_{1/2}$)	0.038(1)
O2 (x,y,z)	**0, 0.5, 0**
O2 ($xs_{1/2}$, $ys_{1/2}$)	0.055(2), 0.018(2)
O2 (ys_3)	0.003(2)
O2 (xs_4)	0.006(3)
O2 (o, oc_1, oc_3, oc_4)	0.64(1), -0.120(8), -0.00(1), 0.04(1)
O2 (U_{11}, U_{22}, U_{33})	0.020(4), 0.017(4), 0.002(5)
GOF (all)	**8.05**
R; main	**9.42**
R; all	**25.40**
# reflections	**3814**
# refined parameters	**23**

For this dynamical refinement, R is the standard measure of quality for the agreement between the calculated and observed intensities, given by the formula [2]

$$R = \frac{\sum |\sqrt{I(obs)} - \sqrt{I(calc)}|}{\sum |\sqrt{I(obs)}|}$$

This was calculated either for all reflections (R; all), or only the main reflections but not the satellite reflections (R; main). The only difference here with X-ray diffraction, is that the calculation of the model intensities is based on dynamical diffraction theory [3], instead of the relation $I = |F|^2$.

For the modulation parameters, s_i and c_i represent the coefficients of the sine and cosine terms of the i^{th} positional modulation wave or occupancy modulation wave (with the prefix "o"). Those coefficients can be positive or negative. If the x and y terms are different, this is explicitly mentioned, e.g. as xs_i. Otherwise the coefficients are identical for x and y.

With x_4 and x_5 as the coordinates of the fourth and fifth dimension, positional modulation waves are given by

$$\mathrm{x}(\mathrm{x}_4) = \sum_i xs_i \ \sin(2\pi i \ x_4) + \ xc_i \ \cos(2\pi i \ x_4)$$

$$\mathrm{y}(\mathrm{x}_4) = \sum_i ys_i \ \sin(2\pi i \ x_4) + \ yc_i \ \cos(2\pi i \ x_4)$$

$$\mathrm{z}(\mathrm{x}_4) = \sum_i zs_i \ \sin(2\pi i \ x_4) + \ zc_i \ \cos(2\pi i \ x_4)$$

and occupancy modulation waves by

$$\mathrm{o}(\mathrm{x}_4) = \ \mathrm{o} + \sum_i oc_i \ \cos(2\pi i \ x_4)$$

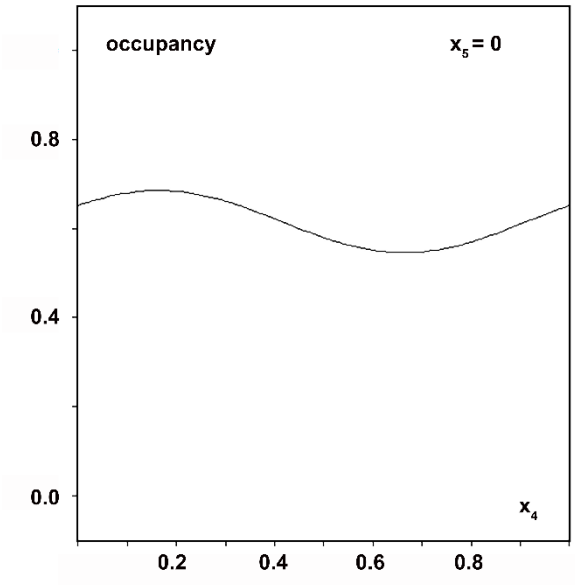

Figure S2: Occupancy modulation function of O2 in function of the fourth coordinate x_4 with $x_5 = 0$; dynamical refinement of ex-situ reduced $La_{0.25}Sr_{1.75}MnO_{4-\delta}$ from precession 3DED.

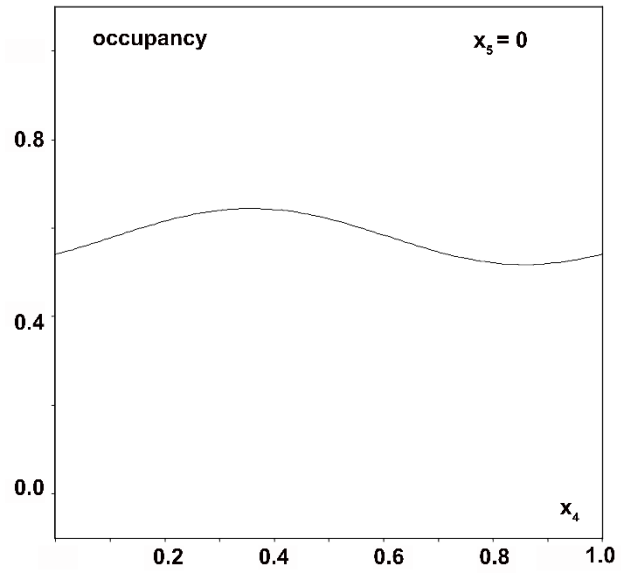

Figure S3: Occupancy modulation function of O2 in function of the fourth coordinate x_4 with $x_5 = 0$; Rietveld refinement of ex-situ reduced $La_{0.25}Sr_{1.75}MnO_{4-\delta}$ from powder XRD.

4.1.1. Comparison Different Space groups Average Structure

Dynamical effects and the dynamical diffraction theory allow 3DED to distinguish between different space groups with identical reflection conditions, by means of the R-value upon dynamical refinement. [2] The table below lists the R-values for the dynamical refinement of the average structure – based on the main reflections only – of modulated $La_{0.25}Sr_{1.75}MnO_{4-\delta}$ with I4/mmm, I4mm, I422 or I4 as a space group.

Space group	**R; main (%)**
I4/mmm	9.80
I4mm	11.25
I422	11.45
I4	14.72

4.2. Rietveld refinement from powder XRD

$La_{0.25}Sr_{1.75}MnO_{4-\delta}$ annealed in 5%H_2/Ar	
La/Sr (x,y,z)	**0, 0, 0.355(1)**
La/Sr (U_{11}, U_{33})	0.001(2), 0.002(3)
La/Sr (s_1)	0.005(6)
La/Sr (c_1)	0.00(3)
La/Sr (U_{13s1}, U_{11c1})	0.01(1), 0.019(8)
La/Sr (U_{33c1}, U_{12c1})	0.02(1), -0.01(1)
Mn (x,y,z)	**0, 0, 0**
Mn (U_{11}, U_{33})	0.001(3), 0.001(3)
Mn (s_1)	-0.01(2)
Mn (o, oc_1)	1.54(6), -0.3(2)
O1 (x,y,z)	**0, 0, 0.16(1)**
O1 (U_{11}, U_{33})	0.07(2), 0.02(2)
O1 (s_1)	-0.01(4)
O1 (zc_1)	-0.01(2)
O2 (x,y,z)	**0, 0.5, 0**
O2 (U_{11}, U_{33})	0.01(4), 0.01(4)
O2 (xs_1, ys_1)	0.04(9), 0.1(1)
O2 (o, oc_1)	0.62(5), -0.1(2)
GOF	**14.45**
R; main	**8.59**
R; all	**9.54**
# reflections	**259**
# refined parameters	**25**

For the refinement from powder XRD, the same standard R-value was used as in the dynamical refinement from electron diffraction, but using the relation $I = |F|^2$ between intensities and structure factors that is not valid for electron diffraction.

5. In-situ gas 3DED: Experimental details

5.1. $Sr_2MnO_{4-\delta}$

For $Sr_2MnO_{4-\delta}$ three different in-situ gas TEM experiments were performed in diluted hydrogen gas. In the first experiment, the sample was heated to 500°C in 5% H_2/He in 1h, after which 3DED was acquired. Then, it was heated to 600°C in another hour. In the second experiment, a prior heating cycle in pure N_2 (heating from 20°C to 500°C in 1h, cooling to 20°C in 1h) was performed to remove moisture and any potentially adsorbed molecules. Next, the sample was heated to 500°C in 5% H_2/He in 1h. After 100', the temperature was increased to 550°C in 30'. Then, the hydrogen concentration was increased to 10% H_2/He after another hour. The sample was left in these conditions for about 16h. After that, the temperature was raised to 600°C in 30', and cooled down again to 550°C in another 30' after taking 3DED series. 30' later the nano-reactor was vacuum pumped to 1.06E-5 mbar at 550°C, and the sample was cooled down to room temperature. At last, another heating cycle to 550°C was performed inside the higher vacuum of the TEM itself (1E-7 mbar). During the preparation of the third experiment, each gas line was vacuum pumped for 3 x 10 minutes (instead of 1x as in the previous experiments). Also, the bottom chip was plasma cleaned with pure argon instead of the 25% O_2/Ar mixture. For the N_2 heating cycle, 550°C was reached in 30', and the sample was kept at this temperature for 1h, after which it was cooled to down room temperature in 2h and kept in nitrogen for 7h. After flowing 5% H_2/Ar for 15', the specimen was heated to 550°C in 30'. Two hours later, the hydrogen content was increased to 10%, and to 25% and 50%, each time after keeping the specimen at this hydrogen concentration for 1h. Another two hours later, pure H_2 was sent to the nano-reactor, and 3h later the sample was cooled down in H_2 to room temperature in 3h. During all previously mentioned stages with constant temperature, 3DED data were acquired. A second heating cycle was performed in pure H_2 overnight without any exposure to the electron beam (heating to 550°C in 90', keeping at this temperature for 8h), but then the chip broke because of a short circuit in the gas supply system. In none of the aforementioned stages of any of the three experiments, 3DED data showed structure transformation away from I4/mmm.

5.2. $La_{0.5}Sr_{1.5}MnO_{4-\delta}$

$La_{0.5}Sr_{1.5}MnO_{4-\delta}$ was subjected to four different in-situ experiments. In the first experiment, it was heated in-situ in the TEM in 5% H_2/He, and 3DED series were acquired at 400°C, 550°C and 700°C. At 700°C, extra reflections appeared in the reconstructed 3D ED patterns that can be indexed as a perovskite structure with a = 3.9 Å. For one crystal, these reflections already emerged from 550°C. Upon cooling back down in 5% H_2/He to room temperature, and heating in 20% O_2/He with 3DED series at room temperature, 250°C and 550°C, the material did not transform anymore. After keeping the sample for one month in air, no further structural changes were seen. In the second experiment with precession 3DED, the same transformation was observed upon directly heating the pristine sample in-situ in 5% H_2/He to 700°C in 1h. Some crystals only showed the transformation upon further increasing the temperature to 750°C. Cooling down to room temperature in 20% O_2/He did not cause any further structure alterations. In a third experiment, pristine $La_{0.5}Sr_{1.5}MnO_{4-\delta}$ was subjected to a desorption heating cycle of 1h at 550°C in pure N_2. Then, sample was heated in 5% H_2/Ar to 550°C at which the temperature was kept for 1h, before increasing the concentration to 50% H_2/Ar. One hour later, this concentration was increased to 100% H_2, and the temperature was raised to 700°C in 20'. After about 16h, the sample was cooled down in pure H_2 to 20°C in 1h. The same transformation was observed during this in-situ experiment as in the previous ones. In the fourth experiment, a molecular sieve (sodium Y zeolite, Sigma Aldrich) and zirconium (Michael Hayward, Oxford) were added to the chip to absorb potential water or oxygen molecules on the surface. Before crushing it, and precipitating and sonicating it in ethanol, the molecular sieve was activated for water absorption by heating in air to 150°C to empty the pores. The sample, Zr and molecular sieve were drop casted onto

the chip in separate droplets to avoid agglomeration. Then, the sample was heated at 3°C/min to 650°C, and cooled back to room temperature at 1°C/min. After that, a faster heating cycle was performed to 690°C (15°C/min) and finally to 700°C (2°C/min). 3DED series were taken at all mentioned intermediate stages. For different crystals, the same perovskite reflections started appearing at different stages of this experiment, leading to the same final structure: a coexistence of the pristine I4/mmm lattice and a perovskite with a = 3.9 Å. However, part of the crystals did not change at all, and kept their pristine structure until the end. For all above mentioned experiments, the perovskite formation was observed equally for crystals that were previously exposed to the electron beam and ones that were not.

5.3. $La_{0.25}Sr_{1.75}MnO_{4-\delta}$

$La_{0.25}Sr_{1.75}MnO_{4-\delta}$ was heated in-situ to 550°C in 5% H_2/Ar in 30', after which 3DED series were acquired. Subsequently, the sample was cooled to room temperature in 5% H_2/Ar in 2h, and left at room temperature in 5% H_2/Ar overnight. Then, it was heated to 700°C in 5% H_2/Ar in 45' and 3DED was performed, after which the sample was cooled to room temperature in 2h30'. During this experiment, the same structural effect was observed as in $La_{0.5}Sr_{1.5}MnO_{4-\delta}$.

5.4. Platinum coating of the heating chip

To try to avoid the reaction of the in-situ heating chips with the samples, coating the chip with a 3 nm platinum layer from a sputtering source was attempted. To optimize the coating thickness, carbon coated copper grids were coated with a platinum layer of 3 nm, 5 nm and 10 nm thickness. 3 nm gave the best diffraction signal. A Python script was written to subtract the Pt rings from the diffraction patterns, allowing to make the reconstructions of crystallographic zones from 3DED. However, when sputtered on the Si_3N_4 chip, the platinum clumped together into crystalline lumps, leaving significant areas of the chips uncovered and thus not protecting the sample against the reaction with silicon. As test samples, $La_{0.5}Sr_{1.5}MnO_{4-\delta}$ and $CaMnO_3$ – which also reacts with the silicon membrane during in-situ experiments – were drop casted in ethanol. The ethanol solution was repelled from the Pt coating window, and rapidly spread over the entire chip. Due to the crystalline lumps, the platinum signal could not be effectively removed from the diffraction patterns, leading to a signal-to-noise ratio of the 3DED data which was too low for processing.

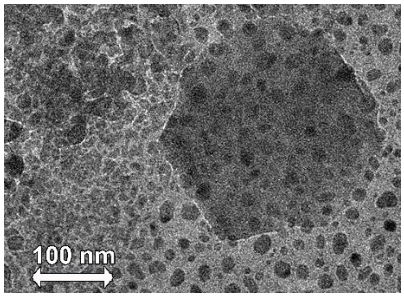

Figure S4: TEM image of $CaMnO_3$ crystal on the platinum coated silicon nitride chip for in-situ heating. The platinum clumped together to form crystalline lumps

6. In-situ gas mono STEM-EELS

An in-situ mono STEM-EELS experiment (mono excited to 0.7) was performed on $La_{0.5}Sr_{1.5}MnO_{4-\delta}$ at 300 kV on a Thermo Fisher Titan^3 aberration-corrected instrument. Dual EELS allowed to simultaneously measure the zero-loss peak and the edges of interest. The sample was first heated in in-situ in pure N_2 to 500°C at 14°C/min and kept at this temperature for 1h while EELS was acquired. Then, it was cooled in N_2 at 14°C/min to room temperature, after which it was heated in 5% H_2/Ar to 350°C at 1°C/min and EELS was acquired at this temperature. After that, the sample was further heated to 550°C in 5% H_2/Ar at 3°C/min. Again EELS was performed. When continuing heating at 7.5°C/min, a sudden leak occurred at 700°C, because of thinning of the windows due to the Si reaction with the sample. This exposed the sample to the vacuum of the TEM. After a few minutes, the sample was quenched in vacuum to room temperature. However, due to the double-chip nano-reactor, the thickness of the support (30 nm + 50 nm + the gas inside the volume) was too thick to obtain a good enough signal-to-noise ratio to make valid conclusions.

References Supplementary Information

[1] Petricek, V. Profile Functions Used in Jana2006. http://jana.fzu.cz/doc/powder_parameters.pdf, visited on January 22 2024.

[2] Klar, P. B., Krysiak, Y., Xu, H., Steciuk, G., Cho, J., Zou, X., Palatinus, L. Accurate Structure Models and Absolute Configuration Determination using Dynamical Effects in Continuous-Rotation 3D Electron Diffraction Data. *Nature Chemistry* **2023**, 15, 848-855.

[3] Palatinus, L., Petricek, V., Correa, C. A. Structure Refinement Using Precession Electron Diffraction Tomography and Dynamical Diffraction: Theory and Implementation. *Acta Crystallographica* **2015,** A71, 235-244.